





RESEARCH ARTICLE | JUNE 01 2023

Shear banding predictions for wormlike micellar systems under a contraction–expansion complex flow

Special Collection: [Tanner: 90 Years of Rheology](#)J. Esteban López-Aguilar   ; Hamid R. Tamaddon-Jahromi  ; Octavio Manero  Check for updates*Physics of Fluids* 35, 063101 (2023)<https://doi.org/10.1063/5.0143432>View
OnlineExport
Citation

CrossMark

Articles You May Be Interested In

Evolution of flow reversal and flow heterogeneities in high elasticity wormlike micelles (WLMs) with a yield stress

Journal of Rheology (May 2023)

Flow of wormlike micellar solutions through a long micropore with step expansion and contraction

Physics of Fluids (January 2020)

Bifurcation in flows of wormlike micellar solutions past three vertically aligned microcylinders in a channel

Physics of Fluids (May 2022)

Shear banding predictions for wormlike micellar systems under a contraction–expansion complex flow

Cite as: Phys. Fluids **35**, 063101 (2023); doi: 10.1063/5.0143432

Submitted: 23 January 2023 · Accepted: 9 May 2023 ·

Published Online: 1 June 2023



View Online



Export Citation



CrossMark

J. Esteban López-Aguilar,^{1,2,a)}  Hamid R. Tamaddon-Jahromi,²  and Octavio Manero³ 

AFFILIATIONS

¹Facultad de Química, Departamento de Ingeniería Química, Universidad Nacional Autónoma de México (UNAM), Ciudad Universitaria, Coyoacán, Mexico City 04510, Mexico

²Institute of Non-Newtonian Fluid Mechanics, Faculty of Science and Engineering, Swansea University, Bay Campus, Fabian Way, Swansea, West Glamorgan SA1 8EN, United Kingdom

³Instituto de Investigaciones en Materiales, Universidad Nacional Autónoma de México, Mexico City 04510, Mexico

Note: This paper is part of the special topic, Tanner: 90 Years of Rheology.

^{a)}Author to whom correspondence should be addressed: jelopezaguilar@unam.mx

ABSTRACT

This study focuses on computational modeling of shear-banded wormlike micellar solutions (WLM) in a complex planar Couette flow, driven by a moving top plate over a rounded-corner 4:1:4 obstruction. The $BMP+_{\tau_p}$ model is used, which is constructed within an Oldroyd-B-like form, coupled with a thixotropic fluidity-based structure equation. Solute energy dissipation drives fluid–structure adjustment in a construction–destruction dynamics affected by viscoelasticity. This model reproduces conventional WLM features, such as shear thinning, extensional hardening/softening, viscoelasticity, apparent yield stress, and shear banding, with a bounded extensional viscosity and an $N_{I\text{Shear}}$ upturn at high deformation rates. The $BMP+_{\tau_p}$ characterization for shear banding is based on extremely low solvent fractions and appropriate shear-banding intensity parameters. Flow structure is analyzed through velocity, stress, and fluidity, whereupon banded and non-banded response is contrasted at appropriately selected flow rates. Solutions are obtained with our hybrid $fe-fv$ algorithm, capturing essential shear-banded flow features reported experimentally. For a fluid exhibiting banding, banded solutions are generated at a flow rate within the flow curve unstable branch. In the fully developed simple shear flow regions, a split velocity profile is observed, with different viscosity bands at equal stress levels, enhanced with a shock-capture procedure. Non-banded solutions are derived for the lowest and highest flow rates sampled, located in the stable branches. Within the constriction zone, banded profiles are lost due to the mixed non-homogeneous deformation. Shear-banding fluids display less intense viscosity/stress features, correlated with their relatively stronger shear thinning response. The constriction resistance provokes a pressure-level adjustment, leading to fully developed Couette-like constant values upstream–downstream.

© 2023 Author(s). All article content, except where otherwise noted, is licensed under a Creative Commons Attribution (CC BY) license (<http://creativecommons.org/licenses/by/4.0/>). <https://doi.org/10.1063/5.0143432>

I. INTRODUCTION

The theme of this predictive finite volume/element modeling study is particularly concerned with investigating material system response of wormlike micellar solutions. These solutions are capable of supporting shear banding under ideal simple shear flow. To further develop and identify the corresponding position adopted in inhomogeneous complex flow, a modified planar Couette flow is considered. This flow is generated by a moving top plate in a rounded-corner 4:1:4 planar contraction–expansion geometry (aspect ratio $\alpha = 4$), see Fig. 1. To avoid singular flow response, the obstruction formed has a rounded tip.

This leads to the observation of pure shear Couette flow in fully developed entry–exit regions, away from the obstruction, while mixed shear-to-extensional flow arises around the contraction zone. This provides the possibility to gather zones of pure shear banding in the entry flow region, allowing us to study the corresponding system response within and beyond the complex flow zone, once exit-flow pure shear conditions are recovered. To suit present purposes, the simplicity of plane Couette flow is preferred (with its single-rate non-SB). The multiple form of rate-profiles, as offered by a pressure-driven deformation, is seen as a more advanced stage in problem resolution, which will appear subsequently.

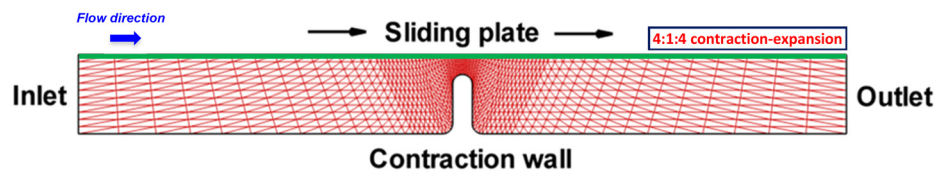


FIG. 1. Schematics of the planar modified Couette geometry—this complex flow geometry is a composition of a 4:1:4 planar contraction–expansion with rounded edges and a drag flow. The flow is promoted by the drag the sliding plate exerts on the fluid stick to its surface. One observes simple shear flow away from the contraction and mixed shear-to-extensional flow in the contraction neighborhood.

Shear-banded flows have been traditionally studied within the restricted context of ideal simple shear flow.^{1–6} In the planar Couette flow under present consideration, shear-banded flow is observed in the form of a discontinuous velocity gradient profile. This profile displays two or more distinct shear rates over multiple bands, which are constant over each band, while simultaneously maintaining equitable total shear stress levels across each band.⁵ This scenario is reflected in an idealized simple shear flow curve, which covers a range of shear rates in the stable branches of the flow curve, each shear rate with its equivalent distinct shear stress level. The level of shear stress itself is determined by the characteristic shear rate U_{plate}/L (which is directly linked to the generated flow rate). Here, U_{plate} represents a moving-wall top-plate velocity, and L is the width of the flow cell. One notes that to generate a banded flow, the overall characteristic shear rate (U_{plate}/L) must lie within the unstable shear rate range regime of the flow curve, which is identified in a negative stress slope, plotted against shear rate rise.^{3,5–7}

Materials that exhibit the phenomenon of shear banding are wide ranging. For example, shear-banded inhomogeneous flow may be observed in aqueous surfactant solutions, pastes, foams, emulsions, granular slurries, liquid crystals, concentrated colloidal emulsions and suspensions, and oil fractions.^{3–6} Despite the large variety of materials capable of displaying bands in complex flow under realistic scenarios and their widespread industrial use, the majority of previous work has been limited to idealized steady simple shear flow. Commonly, this scenario has been analyzed through simple shear Couette flow and Taylor–Couette-type deformations (promoted by surface movement and corresponding drag flow in steady and oscillatory shear protocols).^{3–8} In addition, extension necking has been observed in some wormlike micellar systems,^{9,10} in the form of extensional deformation rate localization, that originates from a multiple-valued extensional stress flow curve, with higher extension rates and pronounced thinning of the filament radius in the midplane of the sample. Despite such advance, there has been a distinct lack of attention paid to the response of banding fluids in complex flow with tangible sparsity in the literature on either experimental or predictive studies.^{11–15} Hence, the present study focuses on inhomogeneous modified Couette flow (with spatial dimension greater than one), and the derivation of numerical solutions for wormlike micellar banding fluids.

Olmsted³ states two general modes of shear banding for shear-thinning and shear-thickening fluids: (i) gradient banding, in which bands of different apparent viscosities coexist, under a common overall shear stress, and (ii) vorticity banding, in which bands with different shear stress distribute in the vorticity direction. Divoux *et al.*⁶ reviewed two main types of soft matter that undergo segregation due to shear banding: (i) fluid-like materials, in which semi-dilute polymeric and

wormlike micellar solutions are grouped; and (ii) soft-glassy materials, which correspond to more concentrated materials than common wormlike micellar solutions, may display liquid or gel-like features (principally yield stress) at rest. These complex fluids exhibit shear banding through a gradient-banding mechanism, which is captured via a non-monotonic flow curve. Such behavior is observed in the experiments of Fischer and Rehage¹⁶ and Pipe *et al.*,¹⁷ where shear stress plateaux are apparent over finite shear rate ranges. In complex flow, particularly in microfluidic planar contractions, Nodoushan *et al.*¹⁵ recently reported intense secondary flow promoted by the interplay of strong shear thinning, shear banding, and yield stress for typical cetyltrimethylammonium bromide/sodium salicylate wormlike micellar solutions.

One of the key features for a model to predict banded flow is its capacity to support a non-monotonic flow curve with localized extrema.^{3,5–7} Two main streams of constitutive modeling have been developed to predict shear banding: a classical approach in polymeric fluids^{18–20} and, alternatively, equations of state based on the description of the fluid microstructure.^{17,21–24}

On the side of polymer-based constitutive models, a modified Johnson–Segalman model characterizes banding materials via a diffusion term in the polymeric extra-stress equation, leading to the so-called d-JS model of Olmsted *et al.*¹⁸ Such stress-diffusion term in the polymeric stress equation has the form of the Laplacian operator of the extra-stress tensor multiplied by a stress diffusivity D , i.e., $D\nabla^2\tau_p$. This particular model choice has captured shear bands in cylindrical Couette flow. In addition, wormlike micellar systems have also been represented through a form of the Giesekus model, where shear banding characteristics are introduced via the non-linear anisotropy coupling parameter.²⁰ These authors developed a method based on large-amplitude oscillatory shear (LAOS) flow, from which fluid characterization could be extracted, and where the onset of shear banding was observed to depend on oscillation frequency.

Within the microstructural constitutive models, an extra structure equation(s) is used to induce non-monotonicity. The Vazquez–Cook–McKinley (VCM) model is one of such, that is based on a discrete form of the “living polymer theory,” attributed to Cates.²¹ This VCM model has been validated in simple flows where rheological homogeneity prevails, and under conditions of shear banding.¹⁷ A closely related model to the VCM model is the Germann–Cook–Beres (GCB) model, under which the structure breakage rate depends explicitly on the trace of the conformation tensor (always positive by definition).^{8,22,23} Moreover, a soft glassy rheology (SGR) model has been proposed recently to model shear banding under LAOS.²⁴ Similarly, solutions for startup in shear with the integral Doi–Edwards model²⁵ have been compared to those obtained by Moorcroft and Fielding,²⁶

with a differential approximation of the Rolie-Poly model. The reactive rod model (RRM) of Graham and co-workers^{27,28} models wormlike micellar solutions as a suspension of rods that interact to form reversible physical bonds that modify the internal structure of the material. This RRM model predicts features of vorticity banding observed in diluted solutions.

In addition, the thixotropic Bautista–Manero–Puig (BMP) models also produce non-monotonic flow curves through their dynamic fluid internal-structure equation. Such an additional fluid–structure evolution equation naturally integrates mechanisms for the construction and destruction of internal structure.^{29,30} This would include a structure destruction coefficient that has an explicit dependence on flow invariants,^{7,12,31} without the complication of handling Laplacian operators. For an approach to modeling shear-banding wormlike micellar solutions, the latest variant is the BMP+ τ_p , which has been used previously under complex flow deformations, such as in circular contraction–expansion²⁹ and flow past a sphere.³⁰ The BMP+ τ_p may be supplemented with a destruction parameter of linear dependence on the second invariant of rate-of-strain tensor, to have the functional capability of generating a non-monotonic curve,³¹ and importantly, a unique solution in the shear-banding (SB) regime. Furthermore, this recent BMP+ τ_p model and some previous variants have incorporated a relationship between fluid structure and viscoelasticity within the structure equation.^{29,30} These developments have resulted in consistent energy-related pressure drop predictions, whereas earlier versions were found to be inadequate.³² In addition to supporting banded flow, the latest BMP+ τ_p model also has a number of attractive rheological features, which include, in shear, a second high-rate upturn in first normal stress difference $N_{1\text{Shear}}$; a bounded extensional viscosity response; alongside extreme shear thinning and strain softening/hardening behavior. These are all properties common to many wormlike micellar systems,^{29,30} which are in agreement with experimental shear flow findings.^{16,17}

On the side of complex flow modeling, Varchanis *et al.*¹⁴ conducted a comparison of the predictive capabilities of well-known models under banding conditions in cross-slot and flow past a cylinder. These authors tested a model proposal based on a fluidity variable against the Johnson–Segalman, the VCM, and the Giesekus models. In addition, López-Aguilar *et al.*¹² and Hooshyar and Germann¹³ carried out predictive work on the flow of wormlike micellar solutions in contraction geometries under banding conditions. Sasmal³³ performed computational modeling of non-banding wormlike micelles in expansion–contraction geometries using the VCM model. In pressure-driven tube flow, Cunha *et al.*³⁴ predicted transient shear banding flow features with a fluidity-based constitutive model.

In this work, a BMP+ τ_p model^{29,30} is used to represent the behavior of wormlike micellar systems under shear-banding conditions, with an ingredient of complex flow posed by the constriction in the modified Couette geometry. This requires an additional term in the constitutive model with viscoelasticity within network–structure destruction kinetics, which can potentially facilitate shear banding. Experimental evidence would indicate that extremely concentrated micellar fluids with non-monotonic shear stress are required to generate shear-banded solutions. Therefore, banded-system response is sought under low solvent fractions of $\beta \leq 10^{-2}$ and material shear-banding intensity parameters of $\zeta > 0$ ($\zeta = 0$, non-banding system), where non-monotonicity is observed in both shear stress and $N_{1\text{Shear}}$.

This article is organized as follows: Sec. II provides details on the BMP+ τ_p model theoretical framework, along with its consequences on the relevant material functions. This is accompanied by a range of suitable deformation rates (converted into their corresponding flow rates Q) that are used to characterize specific instances of low, intermediate, and high deformation rates. One must choose an intermediate deformation rate such that the associated shear stress lies on an unstable branch of the flow curve, while corresponding low and high deformation rates (with equal shear stress) are located in stable branches. The combination of shear rate and banding/non-banding fluids generates the various flow instances, which are analyzed in Sec. III (Numerical Predictions). There, the banded complex flow defines the main findings, while the remaining cases provide a backdrop for direct comparison. Finally, in Sec. IV, the significant findings of the study are summarized.

II. GOVERNING EQUATIONS, CONSTITUTIVE MODELING, AND THEORETICAL FRAMEWORK

A. Conservation principles and BMP+ τ_p model

Wormlike micellar solutions are a type of complex fluids prone to generate banded flows under specific conditions. According to experiments and conventional simple shear flow modeling,^{3,5–7} a combination of factors is necessary to particularly promote exposure to shear banding: first, a deformation-rate dependency on the destruction coefficient; and second, highly concentrated micellar solutions, with solvent fractions on the order of $\beta \leq 10^{-2}$. In this work, the BMP+ τ_p model has been used to characterize the flow of wormlike micellar systems in complex flow.^{29,30} With the BMP family of fluids, non-monotonicity in the flow curve is promoted through an explicit rate-dependent function that acts on the structure–destruction coefficient k of the structure equation, as expressed in Eq. (1).³¹ This function adopts a linear form of the second invariant of the rate-of-deformation tensor II_D , produced by a constant shear-banding intensity parameter (ϑ), viz. $k = k_0(1 + \vartheta II_D)$,

$$\left(\frac{\partial}{\partial t} + \mathbf{u} \cdot \nabla\right)f = \frac{1}{\lambda_s}(1 - f) + k_0(1 + \vartheta II_D) \left(\frac{G_0 \lambda_1}{\eta_\infty + \delta} - f\right) |\boldsymbol{\tau}_p : \mathbf{D}|. \tag{1}$$

The structure equation [Eq. (1)] provides an evolution equation for a dimensionless fluidity $f = \eta_{p0}/\eta_p$ (taken as scaled against a reference viscosity, zero-rate solute-viscosity η_{p0} , with units of Pa·s). This equation establishes a coupled highly nonlinear relationship between the structure dynamics, viscoelasticity, and energy dissipation. Within the structure–destruction term, the shear-banding intensity parameter ϑ appears in the destruction coefficient $k = k_0(1 + \vartheta II_D)$ and modulates the capacity of the fluid to generate banded flows. The ϑ -parameter appears in Eq. (1) in the form of a characteristic time related to the appearance of flow segregation. As a result, a new temporal scale arises, which is closely linked to flow segregation. At sufficiently high solute concentrations, the shear-banding intensity parameter ϑ dictates the appearance of localized extrema (maxima–minima) in the flow curve. Here, the intensity of the shear stress T_{xy} drops, marking a non-monotonic trend in the flow curve, and, then, subsequently rises with deformation rate increase. With $\vartheta = 0$, a monotonic T_{xy} flow curve is recovered. The structure–destruction term contribution to the structure dynamics is modulated through a base constant coefficient

k_0 , with units of inverse of stress (Pa^{-1}). The inverse of constant coefficient k_0 (i.e., k_0^{-1}), is related to a characteristic stress level for structure–destruction. Note that the explicit presence of the relaxation time λ_1 in Eq. (1) quantifies the viscoelastic contribution in the fluid–structure dynamics. Therefore, G_0 represents the elastic modulus at vanishing deformation rates and $(\eta_\infty + \delta)$ is the solute viscosity at high deformation rates. Counterpart structure–construction dynamics is regulated via a structure–construction characteristic time λ_s .

The fluidity f supplies the all-important information on the internal structure of the fluid at hand. It also acts to weight the polymeric stress τ_p contribution in a generalized Oldroyd-B-type differential statement, as follows:

$$\lambda_1 \overset{\nabla}{\tau}_p = 2\eta_{p0} \mathbf{D} - f \tau_p. \quad (2)$$

In Eq. (2), the relaxation time λ_1 also modulates a second source of non-linearity that is related to the upper-convected derivative of solute stress, $\overset{\nabla}{\tau}_p = \frac{\partial \tau_p}{\partial t} + \mathbf{u} \cdot \nabla \tau_p - \nabla \mathbf{u}^T \cdot \tau_p - \tau_p \cdot \nabla \mathbf{u}$.

This complex and highly coupled rheological equation-of-state pairing [Eqs. (1) and (2)] delivers the internal forces within the solute component of such wormlike micellar fluids. It integrates with a complementary solvent Newtonian contribution $\tau_s = 2\eta_s \mathbf{D}$, to generate the total extra-stress $\mathbf{T} = \tau_s + \tau_p$, where η_s is the solvent viscosity. With this information, one seeks to preserve the mass and momentum conservation principles for incompressible and isothermal flow, expressed through the continuity equation and the momentum equation, respectively,

$$\nabla \cdot \mathbf{u} = 0, \quad (3)$$

$$\rho \frac{\partial \mathbf{u}}{\partial t} = \nabla \cdot \mathbf{T} - \rho \mathbf{u} \cdot \nabla \mathbf{u} - \nabla p. \quad (4)$$

Dimensionless forms for Eqs. (1)–(4) and relevant dimensionless group numbers may be obtained by using the following dimensionless variables:

$$\begin{aligned} \mathbf{x}^* &= \frac{\mathbf{x}}{L}, & \mathbf{u}^* &= \frac{\mathbf{u}}{U}, & t^* &= \frac{U}{L} t, & \mathbf{D}^* &= \frac{L}{U} \mathbf{D}, \\ p^* &= \frac{p}{(\eta_{p0} + \eta_s) \frac{U}{L}}, & \text{and} & & \tau_p^* &= \frac{\tau_p}{(\eta_{p0} + \eta_s) \frac{U}{L}}. \end{aligned}$$

Here, U represents a characteristic mean velocity in the contraction gap, originating from the flow rate per unit width Q . L is the width of the flow cell, from which a characteristic deformation rate (U/L) may be defined. Hence, time is non-dimensionalized using the characteristic deformation rate (U/L). Forces, expressed in terms of pressure and stresses, are normalized with respect to the characteristic stress as measured in the first Newtonian plateau, i.e., $[(\eta_{p0} + \eta_s)(U/L)]$. Thus, non-dimensionalization of Eqs. (1)–(4) yields the following dimensionless group numbers: in Eq. (1) and in the form of characteristic times, (i) a dimensionless shear-banding intensity parameter, $\zeta = \vartheta(U/L)$; (ii) a dimensionless structure–construction characteristic time, $\omega = \lambda_s(U/L)$; and (iii) the Weissenberg group number, $Wi = \lambda_1(U/L) = \lambda_1 Q/L^2$, which can be interpreted as an additional viscoelastic dimensionless timescale. Here, λ_1 is taken as 1 s. Alternatively, in Eq. (1), in the form of normalized stresses, (iv) two dimensionless structure–destruction parameters arise, i.e., $\xi_{G_0} = [k_0 G_0 / (\eta_\infty + \delta)](\eta_{p0} + \eta_s)$ and $\xi = k_0(\eta_{p0} + \eta_s)(U/L)$. One of

them, ξ_{G_0} , compares the elastic modulus of the material against its structure–destruction stress, produced with a viscosity ratio. In contrast, ξ normalizes the characteristic total stress at the first Newtonian plateau with respect to the structure–destruction characteristic stress. In addition, from Eq. (2) and T -definition, a solvent fraction $\beta = \eta_s / (\eta_{p0} + \eta_s)$ may be defined. The solvent fraction β expresses a relative measure of the solvent viscosity to the total viscosity at zero deformation rate, i.e., $\eta_{p0} + \eta_s$. β may be used to estimate the relative solvent-to-solute composition in the viscoelastic wormlike micellar solution. The corresponding (variable) viscosity of the wormlike micellar solution is $\eta_{Tot} = \eta_p + \eta_s$. Finally, from Eq. (4), a non-dimensional group Reynolds number, $Re = \rho UL / (\eta_{p0} + \eta_s)$, also arises, based on a material density ρ . The Re number regulates the relative contribution of inertial forces with respect to diffusive forces acting on the material. Inertial force effects are taken as negligible in the present work, i.e., $Re \sim O(10^{-2})$, with its companion implication of inertialess creeping flow.

B. Material functions, flow domain, and alternative deformation rate choices

Figure 2(a) provides the steady-state flow curves for total shear stress T_{xy} against shear rate covering two representative fluids: (i) a non-shear-banding fluid (characterized by a null shear-banding intensity parameter $\zeta = 0$); and (ii) a banding fluid (with $\zeta = 3$), see first column of Table I. The common feature across these data is the need for an extremely low solvent fraction, specifically $\beta = 10^{-2}$, to generate non-monotonic flow curves in the case where $\zeta \neq 0$.^{3,5–7} The characteristic cubic non-monotonic T_{xy} shape in Fig. 2(a) is manifested by the presence of local maxima (rate 10°) and minima (rate 10^1), which allow for the same constant state level of stress to be sustained by two different shear rates.

Furthermore, rheology of interest lies in the shear thinning and extension hardening profiles shown in Fig. 2(b), which are promoted by the set of structure construction–destruction kinetic parameters employed $\{\omega, \xi_{G_0}, \xi\} = \{4, 0.1136, 2.27 \times 10^{-7}\}$ (see Table II, for the full set of parameters used in this work). The extent of thinning covers a rapid drop over two decades, supported by solvent fraction ($\beta = 10^{-2}$). As illustrated in Fig. 2(b), the slope-of-decline is influenced by elevation in shear-banding intensity parameter, where a rise in ζ promotes shear thinning. This is reflected in the power-law index equivalents of $n = 0.196$ for $\zeta = 0$, and $n = -0.142$ for $\zeta = 3$. The negative value of n is associated with stress non-monotonicity.³⁵

Furthermore, in Fig. 2(b), some moderate extensional hardening is detected around unity rates in both shear-banding and non-shear-banding fluids equally, proving to be indistinguishable in this deformation. The position in shear viscosity is reflected through the corresponding response in $N_{I\text{Shear}}$ profiles shown in Fig. 2(c), where the banding fluid displays a characteristic non-monotonic trend in $N_{I\text{Shear}}$, with clear and distinct local maxima (rate 10°) and minima (rate $\sim 10^4$). Notably, the present $\text{BMP} + \tau_p$ model predicts the $N_{I\text{Shear}}$ upturn at high shear rates [observed experimentally in wormlike micellar fluids; see Fig. 2(c)]^{16,17} and also bounded extensional viscosity η_{Ext} response at large extension rates [Fig. 2(b)]. Note that in this analysis, flow and material segregation is promoted primarily through shear deformation. A second alternative for generating banded predictions is currently under development, which involves inhomogeneous

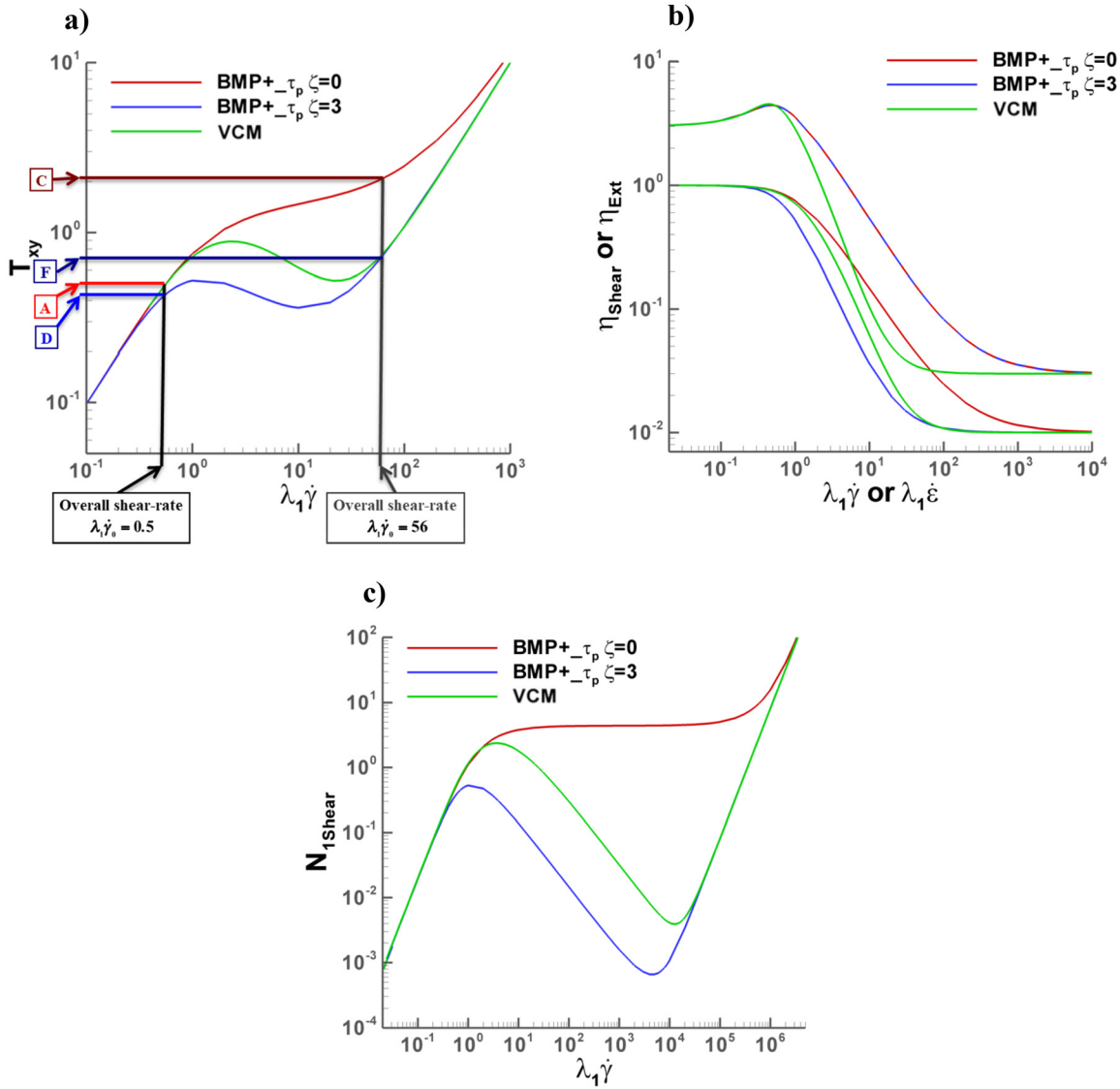


FIG. 2. (a) Shear stress T_{xy} , (b) viscosity, and (c) first normal stress difference in shear $N_{1\text{Shear}}$ against deformation rate (simple shear and uniaxial extension); $\beta = 10^{-2}$; $\text{BMP+}_{-\tau_p}$: $\{\omega, \zeta_{G0}, \zeta, \delta\} = \{4, 0.1136, 2.27 \times 10^{-7}, 1 \times 10^{-6}\}$, non-shear-banding fluid ($\zeta = 0$), shear-banding fluid ($\zeta = 3$); VCM: $\{C_{Aeq}, C_{Beq}, \zeta, \nu, \mu\} = \{0.5, 0.7, 0.42, 7.5 \times 10^{-7}, 1.5\}$. Here, the rheological features provided by the $\text{BMP+}_{-\tau_p}$ model in its shear-banding mode are illustrated. In figure (a), the shear stress vs shear rate $\zeta = 3$ curve displays a non-monotonic trend, characteristic of shear-banded materials (absent for $\zeta = 0$ non-shear-banding fluid); non-monotonicity is also displayed in first normal stress difference response in shear $N_{1\text{Shear}}$, as apparent in figure (c). In figure (b), the corresponding viscosity response is plotted; here, exaggerated shear thinning is observed for the shear-banding $\zeta = 3$ case, being this a common feature of shear-banding fluids. $\text{BMP+}_{-\tau_p}$ model predictions appear comparable against those provided by the well-known VCM model.

TABLE I. Deformation rate vs fluid chart.

	$\lambda_1 \dot{\gamma}_0 = 0.5$ Q = 4	$\lambda_1 \dot{\gamma}_0 = 3.75$ Q = 30	$\lambda_1 \dot{\gamma}_0 = 56$ Q = 450
$\zeta = 0$ non-shear-banding fluid	Case A: non-banded	Case B: non-banded	Case C: non-banded
$\zeta = 3$ shear-banding fluid	Case D: non-banded	Case E: banded	Case F: non-banded

TABLE II. List of parameters.

Parameter (units)	Non-shear-banding fluid	Shear-banding fluid
ζ (–)	0	3
β (–)	0.01	0.01
Ω (–)	4	4
ξ_{G0} (–)	0.1136	0.1136
ξ (–)	2.27×10^{-7}	2.27×10^{-7}
λ_1 (s)	1	1
Re (–)	10^{-2}	10^{-2}

shear and extensional deformations, namely, under extension-necking conditions.^{9,10} Corresponding findings shall be published elsewhere.

An inflected, non-monotonic flow curve [Fig. 2(a)], with predictions for homogeneous simple shear flow, is crucial in generating banded solutions. By examining these non-monotonic flow curves, one can identify an unstable branch, which is characterized by a negative-sloped declining shear stress zone [Fig. 2(a)].^{3,5–7} An unstable branch then stabilizes itself by generating shear bands at the same stress level, but at alternative lower and/or higher shear rates (stable branches, with positive slopes). Each shear band corresponds to a different degree of structure, which can be observed macroscopically as viscosity or fluidity.

$N_{I\text{Shear}}$ banding—in Fig. 3, the rheology is presented for a shear-banding fluid at three different solvent fraction levels. One notes that a plateau in T_{xy} is extracted, with a gradual elevation in solvent fraction, starting from the banding level of 10^{-2} up to 0.05. For $1.0 > \beta \geq 0.05$, the $N_{I\text{Shear}}$ data display band-like features while providing an apparently monotonic trend in shear stress (T_{xy}). The relevant mathematics for this scenario is expounded through the governing solute-content function. This is expressed through the f -functional of Eq. (5) in simple shear flow, where a cubic dependency on shear rate is displayed, affecting stress thereby

$$f^2 - [1 - \omega\xi(1 + \zeta\dot{\gamma})(1 - \beta)\dot{\gamma}^2]f - \omega\xi(1 + \zeta\dot{\gamma})\xi_{G0}Wi\dot{\gamma}^2 = 0. \quad (5)$$

Recall also that the counterpart total shear stress is $T_{xy} = \beta\dot{\gamma} + (1 - \beta)\dot{\gamma}/f$ and the first normal stress difference in shear is $N_{I\text{Shear}} = 2Wi(1 - \beta)\dot{\gamma}^2/f^2$. Unlike previous solutions, as shown and discussed in Fig. 3(b) (with banding promoted by non-monotonic T_{xy}) in the banded regime (case-E), one might ask the question of what flow outcomes are possible under $N_{I\text{Shear}}$ -banding alone. In Fig. 3(c), the fluidity appears relatively larger with β -rise.

In addition, in Fig. 2, a comparison of the rheological response of our BMP+ τ_p is provided against the well-known Vazquez–Cook–McKinley (VCM) model.²¹ This comparison is performed based on similar intensity in the peak of extensional viscosity η_{Ext} -response under $\beta = 10^{-2}$. The parameter set of VCM displaying such behavior is $\{C_{Aeq}, C_{Beq}, \xi, \epsilon, \mu\} = \{0.5, 0.7, 0.42, 7.5 \times 10^{-7}, 1.5\}$. As it is apparent in Fig. 2(b), the BMP+ τ_p and VCM η_{Ext} trends appear similar for low to intermediate extension rates up to the maximum η_{Ext} level, located at $\lambda_1\dot{\epsilon} = 0.5$ units. Beyond this landmark, VCM displays a stronger strain softening trend toward the second Newtonian plateau. Interestingly and relevant to this work, BMP+ τ_p and VCM produce a non-monotonic shear stress flow curve, whose unstable branches are

located in the shear rate range of $1 \leq \lambda_1\dot{\gamma} \leq 30$ units [Fig. 2(a)]. Non-monotonicity is also observed in the first normal stress in shear $N_{I\text{Shear}}$ measure for both models, but over the significantly extended shear rate range of $1 \leq \lambda_1\dot{\gamma} \leq 10^4$ units [Fig. 2(c)]. Notably, in the unstable banding branches, VCM shear and normal stresses always lie at higher levels than those for BMP+ τ_p . As such, one would expect these two models to provide similar banding predictions in complex flow, as has already been reported recently by Varchanis *et al.*¹⁴ A comparative study on predictive capabilities of these and other models in pressure-driven flow through constrictions and past objects will come subsequently, as well as analysis on extension necking situations in stretched filaments of wormlike micellar solutions.

To explore the various disparate regimes of segregated and non-segregated flow, a choice of three key deformation rates $\lambda_1\dot{\gamma}_0$ ($= Wi$) has been made, counterpart to their equivalent global flow rates. Therefore, the imposition of Q , and hence of Wi , implies an imposed target shear rate in the flow curve. Here, low ($\lambda_1\dot{\gamma}_0 = 0.5$, $Q = 4$), intermediate ($\lambda_1\dot{\gamma}_0 = 3.75$, $Q = 30$), high ($\lambda_1\dot{\gamma}_0 = 56$, $Q = 450$) target shear rates $\dot{\gamma}_0$ ($= U_{\text{plate}}/L$) have been imposed. As shown in Table I, each sampled deformation rate then generates its associated flow rate, which is applicable over the entire flow domain. Supporting flow profiles for these shear rate levels are tested on two candidate fluids: one fluid, incapable of supporting flow segregation (with $\zeta = 0$); and a second fluid, prone to generate shear bands (with $\zeta = 3$). The ($\zeta = 3$) fluid may manifest shear-bands in an intermediate shear rate interval of $1 \leq \lambda_1\dot{\gamma}_0 \leq 10$ [Fig. 2(a)]. The stated combination of three key shear rates and two fluids provides six instances to analyze and compare, as recorded in Table I and Fig. 2(a).

C. Flow domain, boundary conditions, ABS-f and centerline VGR corrections, and fe - fv scheme

The flow problem is a modified Couette flow (Fig. 1), where the dragging motion of an upper plate promotes the flow through a planar contraction–expansion geometry. The obstruction has rounded corners and the contraction aspect ratio is $\alpha = 4$. As such, fully developed steady simple shear Couette flow is observed in regions away from the constriction, while inhomogeneous shear-to-extensional mixed flow prevails in the constriction zone.

This modified plane Couette flow has been devised to provide a means of comparison between simple shear flow (in locations away from the constriction) and complex shear-to-extensional flow in the contraction region. Furthermore, in the inlet flow region prior to the constriction, simple shear flow is maintained in the form of a traditional sliding-plate planar Couette flow (as observed in drag flows in co-axial cylinder and cone-and-plate rheometers).^{3–6} In contrast, in the contraction zone, mixed shear-to-extensional deformation prevails, and its effects on the fluid structure are evaluated. Therefore, the simple shear flow is lost due to the presence of the constriction, and yet is recovered downstream of the constriction, where the conditions of simple shear flow are re-established. Such a flow configuration can be found in many industrial devices, such as an extruder, where a molten polymer is carried by blades through an extruder screw, and then pushed through a dye (traditionally studied as a contraction flow), before being shaped or prepared for further processing.³⁶

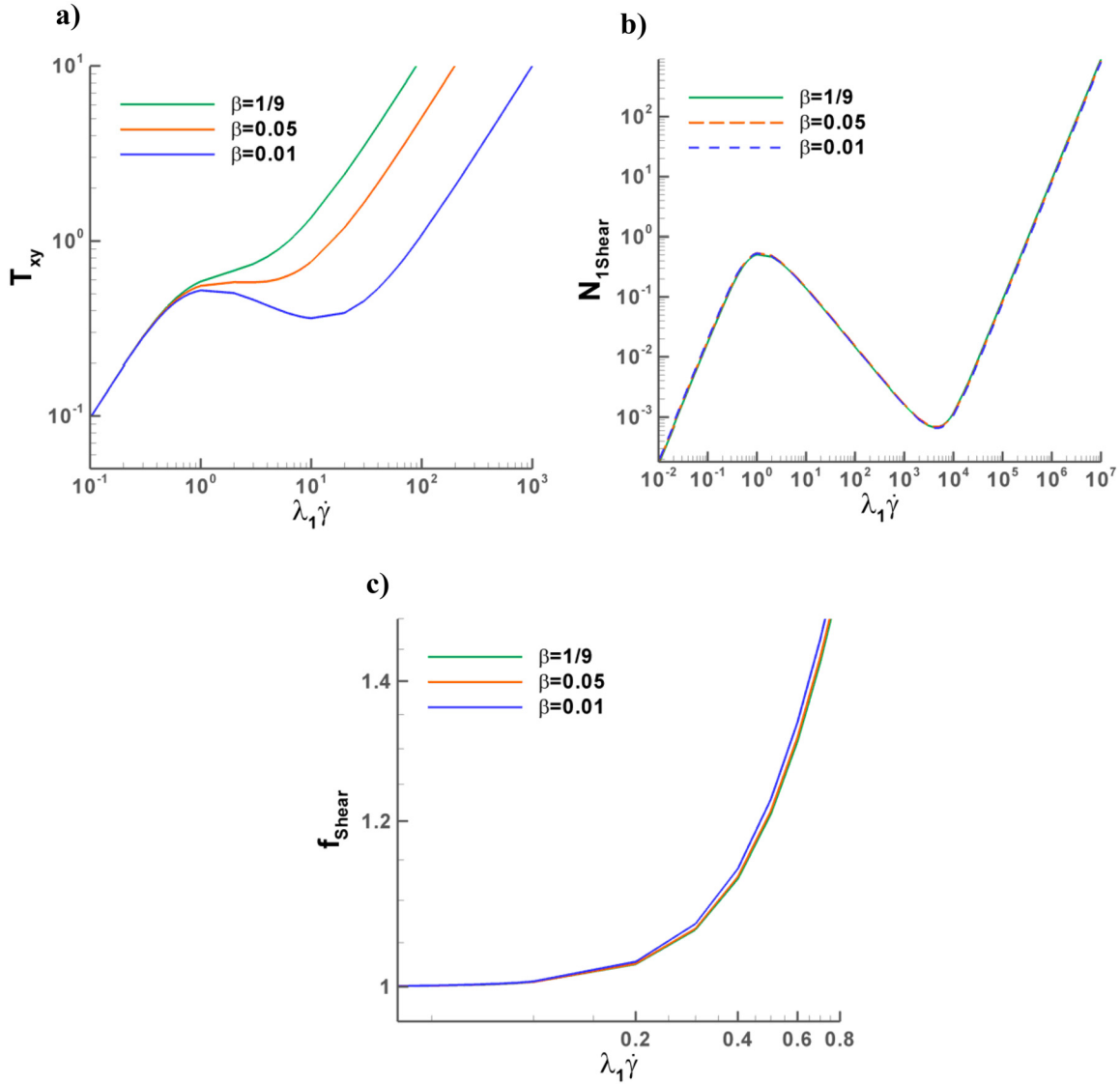


FIG. 3. (a) Shear stress T_{xy} , (b) first normal stress difference in shear N_{1Shear} , and (c) structure parameter f against shear rate (simple shear flow); $BMP+_{-}\tau_p$; $\{\omega, \xi_{G0}, \zeta, \delta\} = \{4, 0.1136, 2.27 \times 10^{-7}, 1 \times 10^{-6}\}$; shear-banding fluid ($\zeta=3$). Under these settings, an illustration is provided on the influence of solvent-fraction variation in the rheological response of the $BMP+_{-}\tau_p$ model. Decrease of solvent fraction signals solute-concentration increase and promotes flow-curve non-monotonicity, as observed in figure (a). Notably, in figure (b), N_{1Shear} -banding features appear invariant with solvent-fraction decrease and are sustained for all solvent fraction β -levels below unity. In terms of the structure parameter in shear f_{Shear} in figure (c), a slight adjustment is observed with β -variation at relatively high shear rates.

1. Periodic boundary condition strategies—banding against non-banding conditions

On the geometry walls, pure shear flow prevails, and the so-called no-slip boundary condition is assumed ($\mathbf{u} = \mathbf{0}$). Linear velocity u_x profiles are specified at the geometry entry–exit, either as piece-wise linear for banding fluids or a single linear for non-banding fluids, respectively. The profiles are determined based on the deformation rate dictated by the flow curve under the sampled shear rate ($\dot{\gamma}_0 = U_{plate}/L$). Particularly important for stability at high deformation

rates, fully developed entry and exit velocity gradient ($\nabla \mathbf{u}$) are observed through feedback/feed-forward procedures, as discussed in López-Aguilar *et al.*^{37,38} Stress (τ_p) is not specified at outlet; hence, the stress is not periodic. In both banding and non-banding scenarios, it is only necessary to set the pressure P at flow-inlet, to impose a pressure level and remove pressure indeterminacy (flow exit attracts Dirichlet setting on velocity). Recall that different constant pressure levels are recorded across upstream and downstream locations. This difference is caused by the presence of the constriction. Consistently, corresponding upstream and downstream fully developed pressure gradients are

null. In practice, it has been found to be more appropriate to specify a pressure level at the inlet, thus avoiding the appearance of any false numerical artifacts in the inlet zone near the wall.

For banding instances:

On velocity profiles, penetration into the field upstream is ensured, from entry to fully developed zone, as well as in the downstream field. This ensures periodicity of the banding flow.

Since the velocity gradient, stress, and f -structure-function are discontinuous under banding and represented by step functions across the banded-velocity zones, it is appropriate to take this into account in the discretization. Starting from continuously extracted solutions, this can be achieved by a series of deferred-correction procedures, which involve incorporating shock-capturing techniques (SCP) to accurately resolve selected variables within each band. Hence, one may appeal to periodic analytic values (constants per band) and use them to iteratively correct fe/fv nodal values throughout the timesteps, within the fully developed flow zones, as and where appropriate. One observes that the interface location between bands generally lies within the control volumes used, so that unique nodal values may be prescribed based on nodal allocation within a specific band.

2. Hybrid finite-element/finite-volume scheme

The numerical method employed is a hybrid finite-element/volume scheme as reported by López-Aguilar *et al.*^{29,30} and references therein. In brief, this scheme is a semi-implicit, time-splitting, fractional three-staged formulation, which invokes finite-element (fe) discretization for velocity-pressure (Q2-Q1, parent-cell) discretization and cell-vertex finite-volume (fv , subcell) discretization for stress. Together, the individual advantages and benefits of both the (fe) and (fv) approximation are combined. The subcell fv triangular tessellation is constructed within the parent fe grid by connecting the midside nodes. Within such a structured tessellation, stress variables are located at the vertices of fv -sub-cells (offering linear interpolation) and solution projection is circumvented. In addition, Galerkin fe -discretization is enforced on the embedded Cauchy component system. The fractional three-staged formulation consists of the momentum equation in stage 1, the pressure-correction equation in stage 2, and the satisfaction of the incompressibility constraint in stage 3 (to ensure higher order precision). On solvers, this leads to a space-

efficient element-by-element Jacobi iteration for stages 1 and 3, whereas for the pressure-correction stage 2, a direct Choleski solution method is utilized. At stage 1 of the stress solution, the discretization using the fv method results in a system that is diagonalized by design, which is immediately amenable to direct solution.

In order to attain numerical solutions under the present highly non-linear flow situations (recall $\beta = 10^{-2}$ and high Q -requirements), the absolute form for the internal structure functional f (termed ABS- f correction) is demanded within the implementation of the constitutive equation. The ABS- f correction arose as a physical argument to ensure thermodynamic consistency, with base on the Second Law of Thermodynamics. This correction poses an absolute value constraint on each term contributing additively to the dissipation function $|\tau_p : D|$ in Eq. (1) and enhances numerical tractability by enforcing consistent material property estimation.³⁷ Recovered velocity gradients, denoted as a VGR correction, are also required to achieve stable numerical solutions over wide ranges of deformation rate, ensuring discrete continuity imposition throughout the flow field.³⁷ Another consequence of the use of the ABS- f and VGR corrections is the conspicuous increase in the level of non-linearity at which numerical algorithms loose tractability, traditionally denoted as a critical Weissenberg number Wi_{crit} . López-Aguilar *et al.*^{37,38} recorded Wi_{crit} increments of $O(10^3)$ on solutions obtained using the ABS- f /VGR doublet, with respect to simulations devoid of such corrections. Moreover, the ABS- f correction has been found to be generally applicable to other families of constitutive equations such as PTT and FENE.^{37,38}

López-Aguilar *et al.*³⁸ recently reported on mesh characteristics and a mesh refinement study for the 4:1:4 planar contraction-expansion with rounded edges geometry in Fig. 1, as well as for the rheological equations of state in the Bautista-Manero family and the solution algorithm. To complement such mesh-independence information with the problem to hand, BMP+ τ_p solutions captured in the fully developed flow regions in the banding regime are illustrated in Fig. 4. Here, node-element density is increased in the velocity gradient direction, where construction of the coarse and the refined meshes display half and twice the number of elements, respectively, that the medium mesh has cross stream. The solution-capture test is performed in terms of the banded shear and normal stress profiles, as well as the location of the band interface. The chosen fluid is case-E, capable to displaying banding under parametrization $\{\beta, \omega, \xi_{G0}, \xi, \delta\} = \{10^{-2}, 4, 0.1136, 2.27 \times 10^{-7}, 1 \times 10^{-6}\}$,

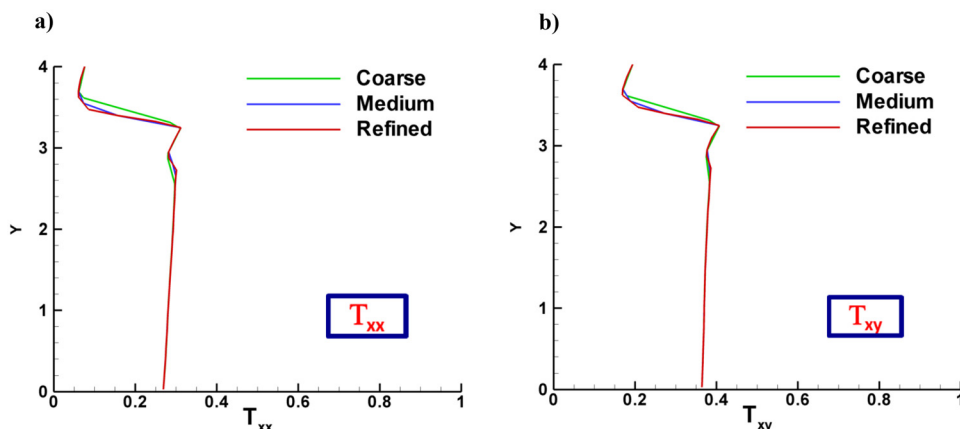


FIG. 4. (a) Normal stress T_{xx} and (b) shear stress T_{xy} profiles sampled at the upstream fully developed region; $\beta = 10^{-2}$, $\{\omega, \xi_{G0}, \xi, \delta\} = \{4, 0.1136, 2.27 \times 10^{-7}, 1 \times 10^{-6}\}$; mesh-refinement study for coarse, medium, and refined grids; case E: shear-banding fluid ($\zeta = 3$).

2.27×10^{-7} , and 1×10^{-6} }. In general, solutions appear well-resolved as the location of the band interface remains invariant across mesh densification. The medium and refined solutions approximate the interface location well, which was found to be at $y_{int} \sim 3.48$ units for the test case. The normal and shear stress profiles have similar shapes and intensities, particularly on the refinement step from medium to refined. However, some localized noise is noted near the interface. This noise is due to the discontinuity posed by the interface and solution approximation. This is dealt with via a shock-capture implementation, which is discussed in detail in the results section. Hence, from this point on, the medium mesh is considered for the solution description.

III. NUMERICAL PREDICTIONS

In this section, the solutions for the cases in Table I demonstrate the ability of our $BMP+_{-}\tau_p$ constitutive model and our numerical algorithm to generate banded or non-banded flows in the fully developed region away from the constriction. These solutions also illustrate the influence of the obstruction and its mixed shear-to-extensional deformation fields on the attained flow structure.

Particularly for the ($\zeta = 3$) banding fluid, an intermediate flow rate ($Q = 30$) lies within the shear-banding deformation rate range, making banded solutions possible. The lowest ($Q = 4$) and highest ($Q = 450$) flow rates lie outside the shear-banding regime, where non-banded solutions are expected. In the following sections, details on the development of these instances are provided.

A. Banded against Non-banded solutions—intermediate target flow rate ($\lambda_1 \dot{\gamma}_0 = 3.75$), shear-banding fluid case-E against non-shear-banding fluid case-B

1. Case-E banded velocity- u_x and structure (viscosity and structure-parameter- f) fields and profiles

First, the $\zeta = 3$ -banded Case-E is considered (Table I), for which the corresponding velocity u_x -field is presented in Fig. 5(a). The nature of this complex planar flow reveals simple shear flow away from the contraction, and a combined shear-to-extensional deformation in the contraction region. As such, several key features may be observed and discerned from these two deformation states. In the upstream and downstream fully developed flow regions, one can observe a banded steady-state velocity u_x field, with velocity bands appearing in the vertical y -spatial direction. The banded flow pattern is then lost as the fluid approaches the constriction. Subsequently, one notes that, after traversing through the constriction and upon recovering simple shear deformation, a banded fully developed flow pattern is recovered.

In Fig. 6(a), flow segregation is recorded through a split u_x profile. This is sampled cross-stream at a fixed horizontal x -spatial coordinate in the upstream fully developed flow region [one notes the null transversal velocity u_y -profile in Fig. 6(b)].

The interface between bands is located at the inflection point of such a split u_x -profile ($y_{int} \sim 3.48$ units), where there is a sharp change in color intensity in the fields [Fig. 5(a)]. Such an interface can be determined using the lever rule,^{6,31} to lie at a location of: $y_{int} = [(\dot{\gamma}_2 - \dot{\gamma}_0)/(\dot{\gamma}_2 - \dot{\gamma}_1)]\alpha_d$, where $\dot{\gamma}_0$ is the target characteristic shear rate and $\alpha_d = 4$ units is the distance that separates the moving plate and the contraction wall. Here, $\alpha_d = 4$ also corresponds to the contraction ratio in this contraction–expansion geometry. As such, $\dot{\gamma}_0 = 3.75$ and

$T_{xy} \sim 0.4$ units [Fig. 7(a)], in this case, it is located in the unstable non-monotonic shear stress regime.

Then, extracted from the flow curve at an equivalent shear stress level, $T_{xy} \sim 0.4$ units, $\dot{\gamma}_1 = 0.5$ units, and $\dot{\gamma}_2 = 27$ units are the low and high shear rate stable branches, respectively. Each band, which constitutes the split u_x profile, is then supported by its corresponding shear rate, with the low- $\dot{\gamma}_1$ and high- $\dot{\gamma}_2$ shear rates being assigned to the lower and upper bands, respectively. Then, the narrow upper-band in the local neighborhood of the moving plate [with a red/intense-core; Fig. 5(a)] represents the material in the high- shear rate band. In terms of rheological response [Fig. 7(b)], this high- $\dot{\gamma}_2$ shear rate band corresponds to a highly unstructured fluid of total viscosity $\eta_{Tot} \sim 1.8 \times 10^{-2}$ units [see blue band in viscosity field in Fig. 5(c) and counterpart red-fringe in the structure–parameter f -field of Fig. 5(d)]. In contrast, the low- $\dot{\gamma}_1$ shear rate band occupies the remaining channel space, lying between the band interface and the bottom geometry wall [homogeneous blue band in f -field of Fig. 5(d)]. Here, a highly structured fluid is reported, with a viscosity of $\eta_{Tot} \sim 0.8$ units [as indicated by the orange band in viscosity field in Fig. 5(c)].

In the complex flow region, the pre-banded flow field is disrupted and distorted by the constriction, with unstructured material flowing through the constriction gap, while highly structured material occupies the stagnant corners [as shown in the viscosity field representation, Fig. 5(c)]. In Fig. 6(d), the cross-stream velocity U_x -profile in the contraction gap displays changes of slope near the contraction and top walls, fact that reflects the non-homogeneity of the flow in the contraction region. Then, beyond the constriction, and once the fluid viscosity has had the opportunity to readjust, a banded morphology is reformed (nb. the downstream intermediate-green viscosity color levels, illustrate convection downstream).

A clarification is worthwhile regarding the meaning of the terms “inhomogeneous deformation” and “inhomogeneous flow” for the rheological community. In complex flows studied under the umbrella of non-Newtonian fluid mechanics, “inhomogeneous flow/deformation” refers to a flow in which simultaneous shear and extensional deformations are mixed in the domain. In contrast, in rheometry, where shear banding has traditionally been studied, an “inhomogeneous field” refers to fields with fluid segregation (bands) in a simple shear deformation. Hence, in this paper, to address this issue, we differentiate and define the concept of “complex flow” as a mixed inhomogeneous shear-to-extensional deformation. Additionally, we define “banded flow” as a flow that supports the coexistence of two bands of material with different physical properties, i.e., viscosity.

2. Case-E-banded shear and normal stress fields and profiles, and pressure field

The fully developed banded velocity-profile response of $\zeta = 3$ solution is accompanied by a roughly constant shear stress T_{xy} field [Fig. 5(e)]. Notably, at the channel height where the interface between the bands appears, a horizontal strip of slightly larger T_{xy} values is apparent. The counterpart T_{xy} profile reveals a constant T_{xy} level [~ 0.4 units; Fig. 6(c)], which appears throughout the flow gap. Precisely near the interface location, the T_{xy} profile oscillates about the mean level. This is consistent with the discretization and the discontinuous nature of the shear rate profile across the flow gap, which ideally necessitates shock-capturing techniques for more accurate resolution

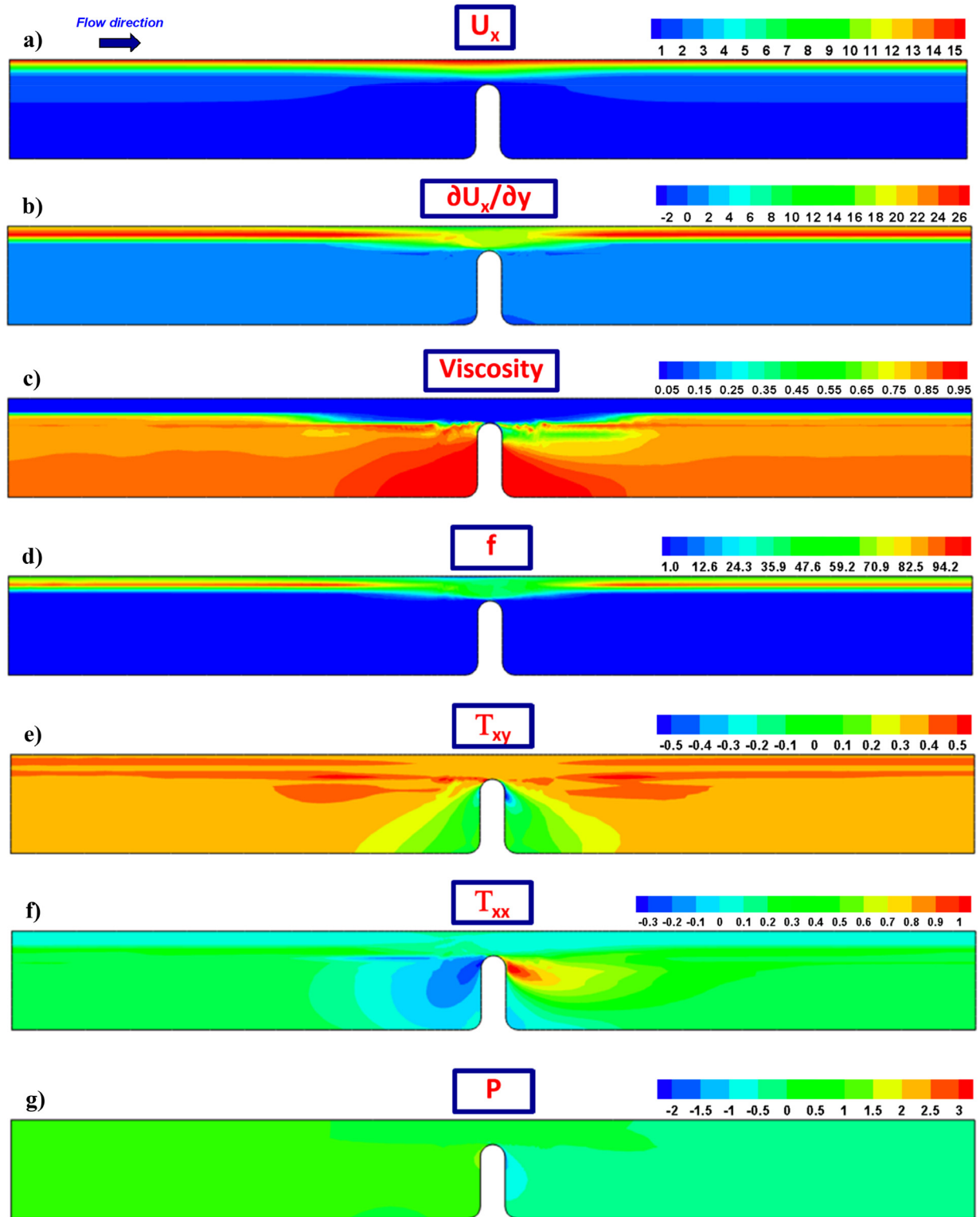


FIG. 5. (a) Velocity U_x , (b) shear rate $\partial U_x / \partial y$, (c) viscosity, (d) f -functional, (e) shear stress T_{xy} , (f) normal stress T_{xx} , and (g) pressure P fields; $\beta = 10^{-2}$, $\{\omega, \zeta_{G0}, \zeta, \delta\} = \{4, 0.1136, 2.27 \times 10^{-7}, 1 \times 10^{-6}\}$; case E: shear-banding fluid ($\zeta=3$).

Fully-developed & inlet profiles

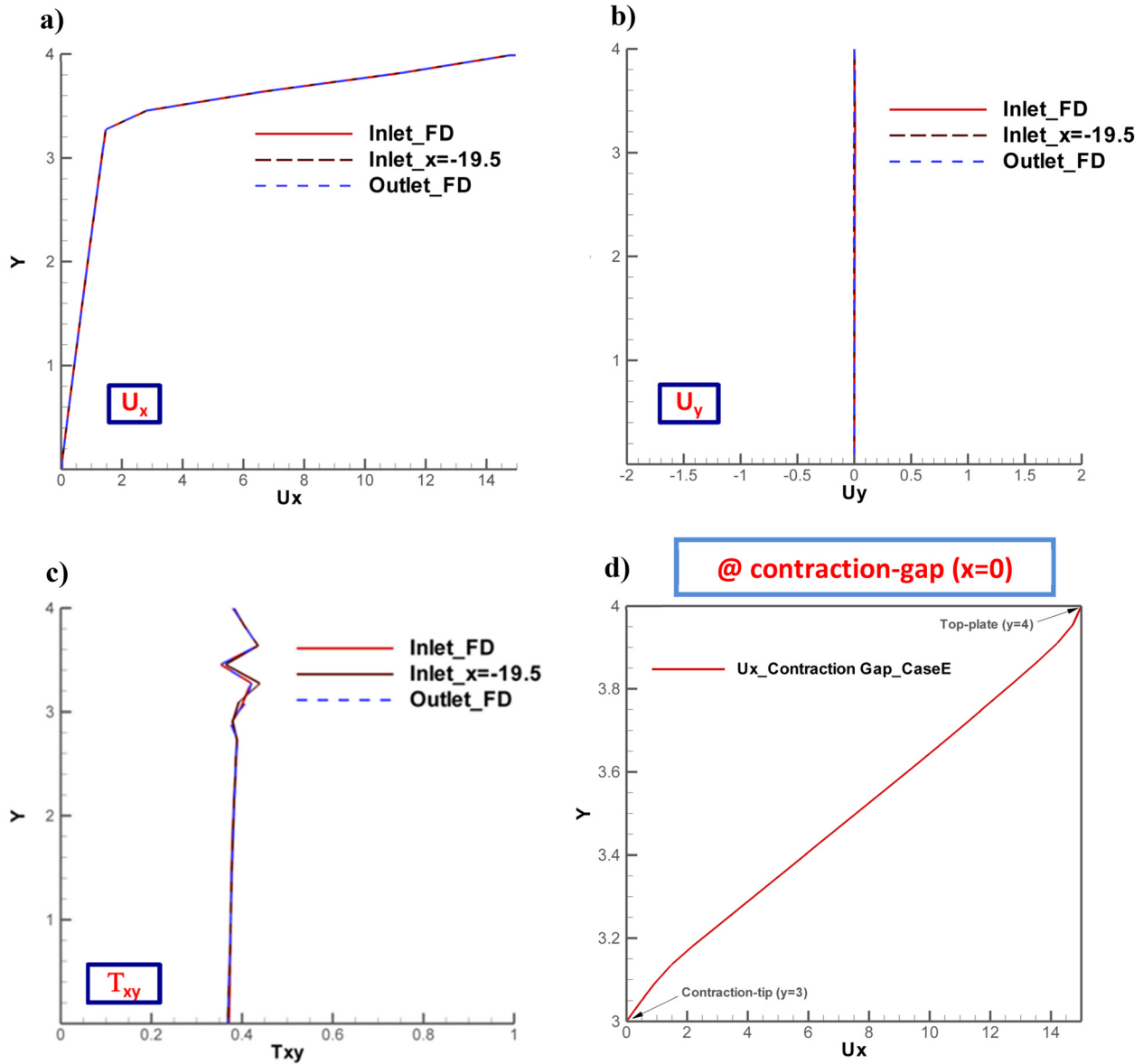


FIG. 6. Profiles of (a) velocity in x -direction U_x (b) velocity in y -direction U_y , (c) shear stress T_{xy} and (d) U_x @ contraction gap; $\beta = 10^{-2}$, $\{\omega, \zeta_{G0}, \zeta, \delta\} = \{4, 0.1136, 2.27 \times 10^{-7}, 1 \times 10^{-6}\}$; case E: shear-banding fluid ($\zeta = 3$).

(see earlier remarks). These undulations coincide with the slightly more intense strips observed and may be associated with the discontinuity posed by the interface (see on with shock-capturing). Conspicuously, the normal stress T_{xx} also inherits bands, driven by the velocity profile [Fig. 5(f)]. Such banding in normal stress components has also been observed in non-extensional large amplitude oscillatory shear (LAOS) predictions using the Rolie-Poly model.³⁹ Once more, the homogeneous T_{xy} field and the inhomogeneous T_{xx} response in

the fully developed regions are disturbed by the presence of the constriction [Figs. 5(e) and 5(f)]. Here, the effects of the combined shear-extensional deformation are more evident. On T_{xy} , the stripped interface disappears and a homogeneous T_{xy} level is adopted in the constriction gap [Fig. 5(e)]. Moreover, in the recess zones, there are triangular green structures, and a localized small blue zone emerges on the contraction back face, near its tip. Consistently, on T_{xx} , two colored-level regions are reported, with base on the contraction tip of

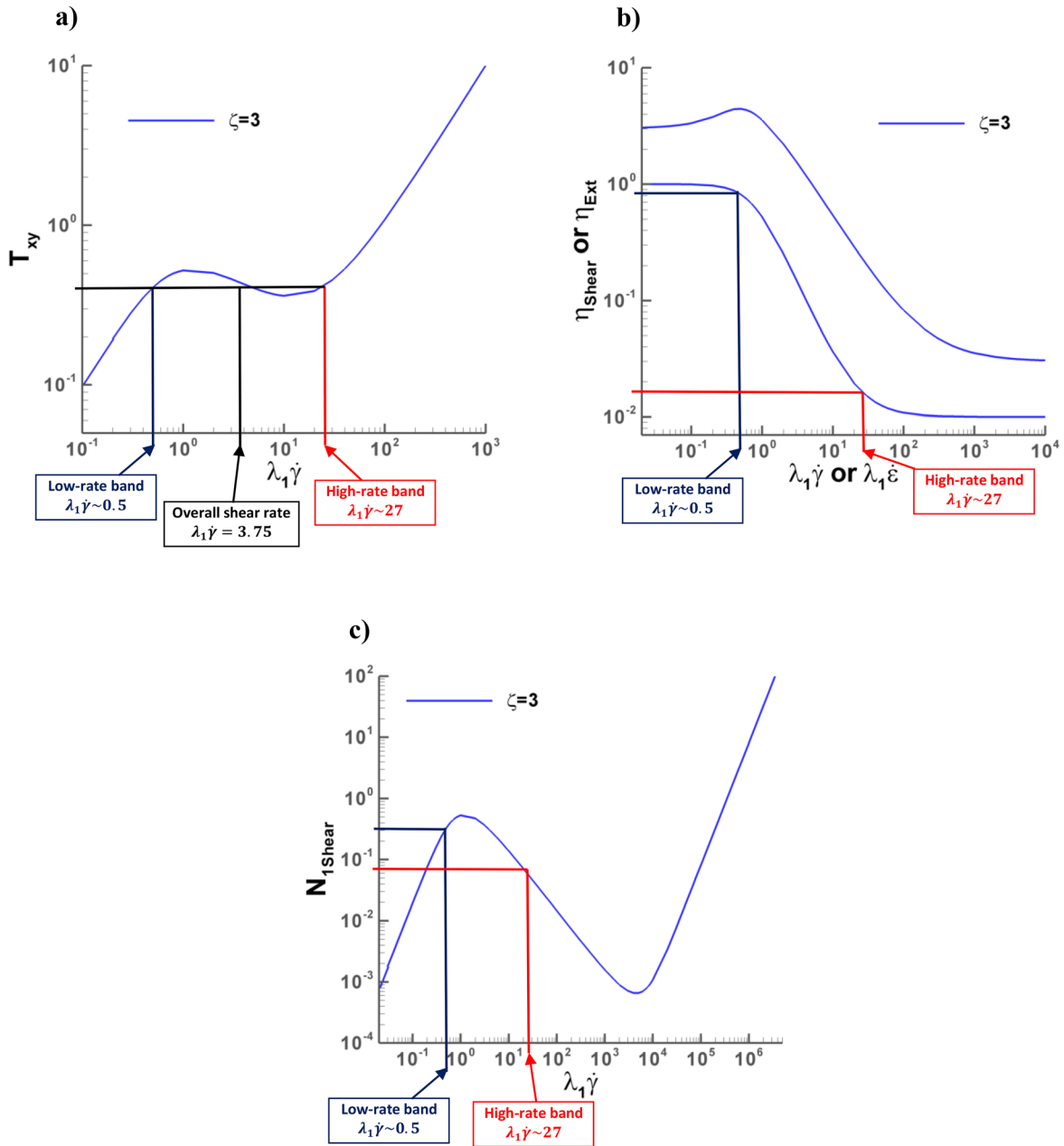


FIG. 7. (a) Shear stress T_{rz} , (b) shear viscosity η_{Shear} and extensional viscosity η_{Ext} , and (c) first normal stress in shear $N_{1\text{Shear}}$ against deformation-rate (simple shear and uniaxial extension); $\text{BMP}+_{-\tau_p}$; $\beta = 10^{-2}$, $\{\omega, \zeta_{G0}, \zeta, \delta\} = \{4, 0.1136, 2.27 \times 10^{-7}, 1 \times 10^{-6}\}$; case E: shear-banding fluid ($\zeta = 3$).

negative-blue values upstream and a positive-red counterpart downstream [Fig. 5(f)].

In case E, the pressure sustaining flow passes from a green-uniform base pressure level to a relatively low and brighter-green pressure level downstream of the contraction [Fig. 5(g), $P_{\text{outlet}} / (1 + P_{\text{inlet}}) \sim 5 \times 10^{-1}$]. Note that in the upstream and downstream fully developed regions, pressure fields appear independent of the main-flow x direction, consistent with Couette deformation. The

upstream-to-downstream pressure-level adjustment is provoked by the mixed shear-to-extension flow within the constriction.

From such a continuous solution representation, deferred-correction solutions may be considered when incorporating shock-capturing (SCP) across the bands to more directly address solution discontinuity and its localization. The effectiveness of this strategy may be demonstrated by comparing cross-stream profiles of solution refinements with no-shock-capturing solutions. Here, the entry SCP

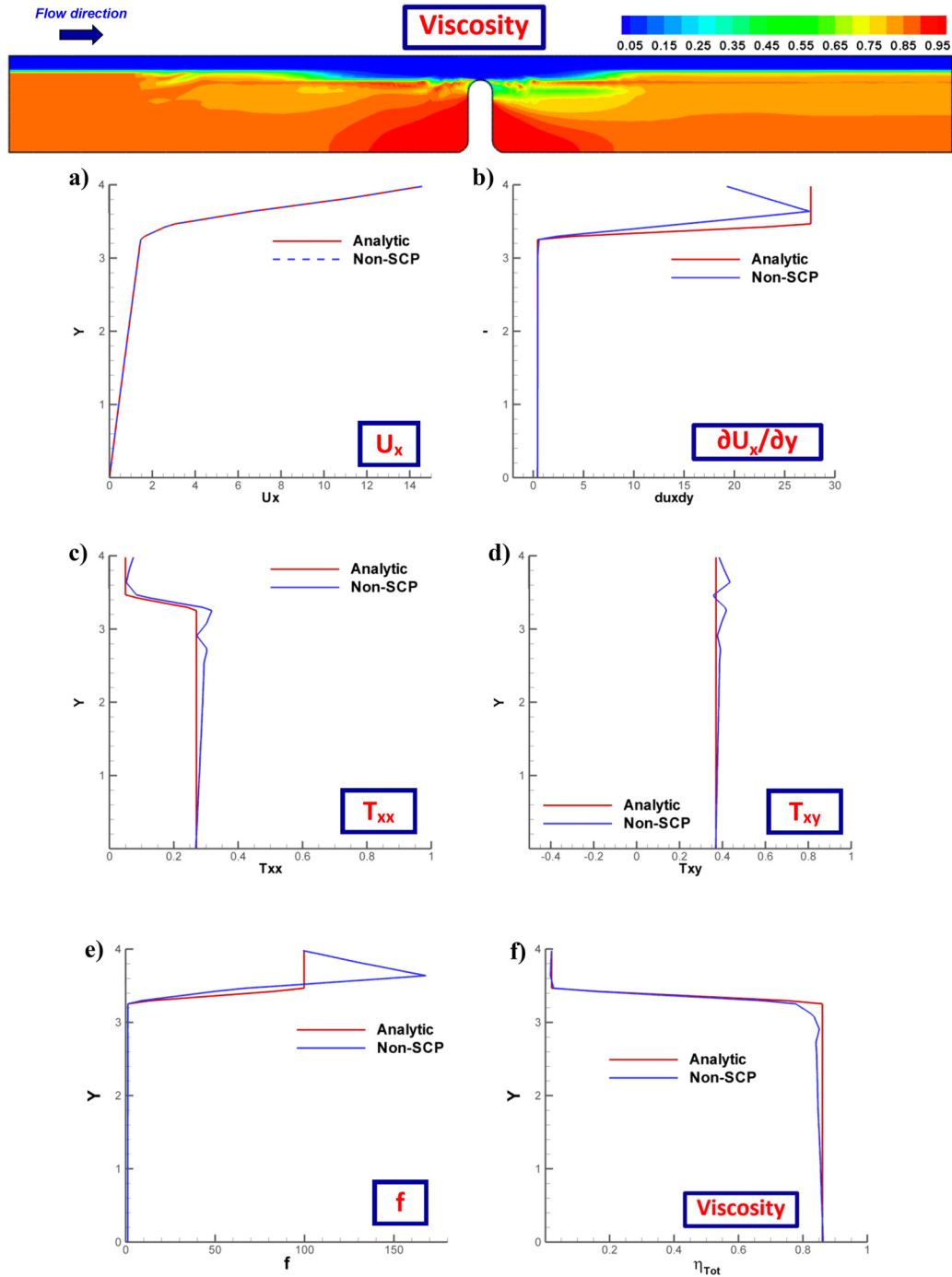


FIG. 8. Banded-solution profiles: entry-analytic vs exit-non-SCP; (a) velocity U_x , (b) shear rate $\partial U_x/\partial y$, (c) normal stress T_{xx} , (d) shear stress T_{xy} , (e) f -functional, (f) viscosity; $BMP+\tau_p$; $\beta = 0.01$, $\{\omega, \zeta_{G0}, \zeta, \delta\} = \{4, 0.1136, 2.27 \times 10^{-7}, 1 \times 10^{-6}\}$; case E: shear-banding fluid ($\zeta=3$).

conditions are set as analytic in velocity gradient and stress, which imposes the f -structure-function (Fig. 8). The exit SCP conditions are then taken as follows: first, by imposing periodicity on the f -structure-function; second, by imposing periodicity on velocity gradients;

third, by imposing periodicity on both; then, stress is computed as before. The corresponding exit-flow SCP solutions are provided in Fig. 9, for both major stress components (T_{xy} , T_{xx}). Through these solutions, one can contrast the analytic entry SCP conditions. Here, the

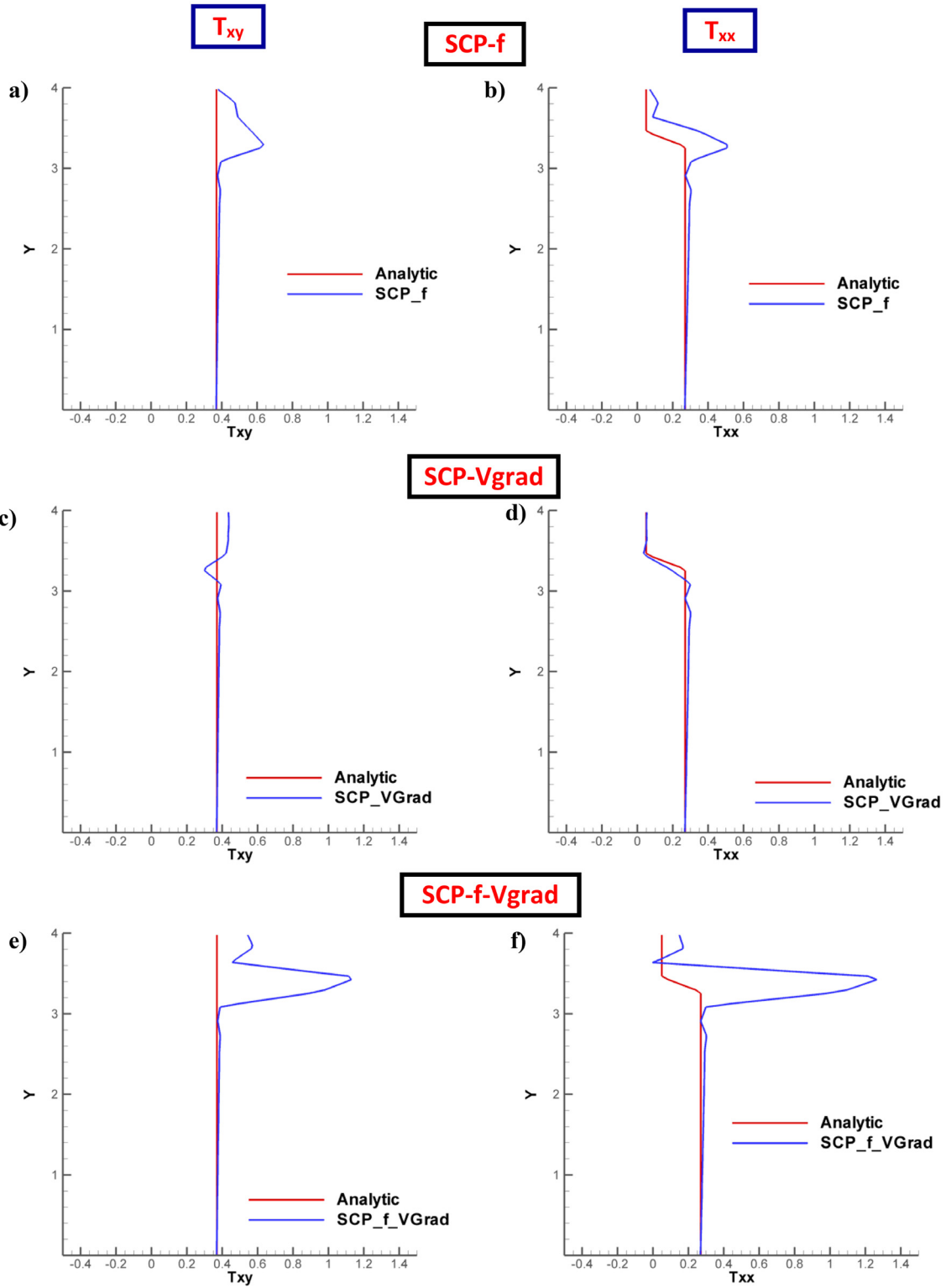


FIG. 9. Banded-solution profiles under shock capture (SCP): analytic-entry vs exit-SCP; SCP-f: (a) shear stress T_{xy} , (b) normal stress T_{xx} ; SCP-Vgrad: (c) T_{xy} , (d) T_{xx} ; SCP-f-Vgrad: (e) T_{xy} , (f) T_{xx} ; $BMP+_{-}\tau_{pi}$; $\beta = 0.01$, $\{\omega, \zeta_{G0}, \zeta, \delta\} = \{4, 0.1136, 2.27 \times 10^{-7}, 1 \times 10^{-6}\}$; case E: shear-banding fluid ($\zeta = 3$).

04 September 2023 10:38:04

major correction influence is from periodicity in the velocity gradients. Any correction from the f -structure-function (alone/in combination with velocity gradients) is seen to deteriorate the quality of exit-stress profiles. In these data, the overall quality of the none-shock-captured solution is also complemented.

2. Case-B-non-banded velocity field

For case B (non-shear-banding fluid $\zeta = 0$; Table I and Fig. 10) and in contrast to case E ($\zeta = 3$, Fig. 5), the fully developed velocity u_x field now appears as a single and continuous shear rate form, as shown in Figs. 10(a) and 10(b). This is accompanied by upstream-downstream constant non-segregated T_{xy} and T_{xx} levels [Figs. 10(e) and 10(f)]. Such a linear upstream velocity profile is lost in the constriction zone, where the fluid is accelerated as a consequence of the converging flow. Here, the T_{xy} field develops strongly positive and negative localized regions attached to the contraction walls, and a negative elongated region on the moving plate [Fig. 10(e)]. The normal stress T_{xx} field presents a strong elastic zone in the contraction region [Fig. 10(f)], followed streamwise by a negative zone whose influence appears to be convected downstream. In the upstream recess zone, there is an additional negative-strong patch, which is balanced downstream by an isolated red-positive core that elongates into a tail downstream.

In terms of fluid structure and away from the constriction zone, the viscosity (and its counterpart structure-parameter- f) distribution remains at a single constant level upstream [Figs. 10(c) and 10(d)]. Then, as the fluid approaches the contraction, the varied and distributed deformation rate breaks down its structure, resulting in an asymmetric blue-low viscosity region filling the constriction. In the deceleration zone beyond the constriction, the material is observed to recover its structure. This fact is witnessed, via the viscosity field, by a sudden change from a highly unstructured fluid (blue), to a more structured fluid (green). This is expressed through two elongated arms directed downstream, one sticking to the moving plate and the other located in the middle of the domain.

In the recess zones, there are isolated red/high viscosity triangular-shaped zones, suggesting relatively slow motion in these vicinities. Here, due to the highly nonlinear conditions based on solvent content ($\beta = 10^{-2}$) and increased flow rate, the pressure drop required to drive the flow is enforced through a fixed-pressure boundary condition at the inlet. This implies that the resulting pressure level must be calculated at the flow outlet. Such a procedure ensures that no downstream blockage is created in pressure, which may otherwise degrade the downstream solution quality in taking up fully developed flow conditions. The ensuing pressure field passes from one of a characteristic constant-pressure Couette flow upstream [Fig. 10(f)] to a similar form downstream. Afterward, a pressure build-up (pressure-gradient, ~ 19.9 units) sustains the flow through the constriction.

B. Non-banded solutions at low flow rate—A against D cases

1. Case-A and case-D non-banded solutions at low deformation rates

Considering low deformation rates ($Q = 4$; $\dot{\gamma}_0 = 0.5$), the instances of the shear-banding fluid ($\zeta = 3$; case-D), which lies outside the unstable branch of the flow curve [Figs. 11(a) and 11(b)], and the non-shear-banding fluid ($\zeta = 0$; case-A), the predictions indicate single-

banded u_x fields [Figs. 12(a) and 12(b)]. Across both instances (A and D), and at this relatively low state of deformation, solutions adopt a similar form, with only slight level differences detected in the constriction gap. In the fully developed regions, the single-banded velocity profiles are supported by uniform states in T_{xy} and T_{xx} stress fields [Figs. 11(e) and 11(f) and 12(e) and 12(f), respectively]. Notably, the shear-banding ($\zeta = 3$; case-D) fluid solution set yields less intense features, with a single green-level apparent around the constriction zone. Correspondingly, the non-shear-banding ($\zeta = 0$) case-A solution sustains intense stress levels. These differences may be correlated with the relatively larger shear and normal stress levels for the non-shear-banding A-fluid [indicated in Fig. 2(a)]. Recall that non-zero shear-banding intensity parameters $\zeta \neq 0$ provoke exaggerated shear thinning features [see shear rate differences in Figs. 11(b) and 12(b)].

This low flow rate ($Q = 4$; $\dot{\gamma}_0 = 0.5$) has been chosen to impose a stable branch deformation rate in the flow curve, while still maintaining some differences between shear-banding and non-shear-banding fluids. Here, for the shear-banding fluid ($\zeta = 3$), one can observe a slightly lower T_{xy} level compared to the non-shear-banding ($\zeta = 0$) case. This ($\zeta = 3$) decline in T_{xy} slope is related to the proximity to the flow curve maxima at higher shear rate levels.

In terms of fluid structure, for case-D ($\zeta = 3$) viscosity and f fields [Figs. 11(c) and 11(d)] reflect liquefied material in the constriction zone, while it is fully structured in the recess zones (red levels). The extremes in viscosity distribution noticeably spread and fill the constriction zone (blue levels), while relatively smaller viscosity levels occupy the fully developed regions [green-shading, Figs. 11(c) and 11(d)]. In contrast in Figs. 12(c) and 12(d), case A ($\zeta = 0$) viscosity fields display a relatively structured material away from the constriction (red levels) and isolated thinned-blue fluid patches that have base on the contraction tip and the wall. They only influence the material from around the constriction zone.

This distinct change in structural behavior can be attributed to the exaggerated shear-thinning properties of the shear-banding case-D ($\zeta = 3$) fluid. At a fixed shear rate (beyond $\dot{\gamma}_0 \sim 0.3$), the shear-banding case-D ($\zeta = 3$) fluid produces a less-responsive system, with relatively low levels of material change than those of the non-shear-banding case A ($\zeta = 0$) fluid. This can be observed from the rheology of the flow curve in Fig. 2(a) when comparing the field solutions of case A and case D. The only caveat to this statement lies in the pressure field, both around and downstream of the constriction, which is significantly more disrupted under the shear-banding case D ($\zeta = 3$) fluid [Fig. 11(g)] than for the non-shear-banding case A ($\zeta = 0$) fluid [Fig. 12(g)].

C. Non-banded solutions at high flow rate—C against F cases

1. Case C and case F non-banded solutions

In the alternative extreme of high deformation rate, the second stable branch of the flow curve is located, as shown by solutions at ($Q = 450$; $\dot{\gamma}_0 = 56$) [Fig. 2(a)]. Therefore, in the non-shear-banding ($\zeta = 0$) case C solution (Fig. 13), a strong single-banded u_x field is captured away from the constriction. In the complex flow constriction region, intense activity is recorded through stress T_{xy} and T_{xx} zones, which are based on the contraction tip and around the moving wall [Figs. 13(e) and 13(f)]. Here, the large velocity of the moving wall causes increased kinematics stimulated to convect downstream the

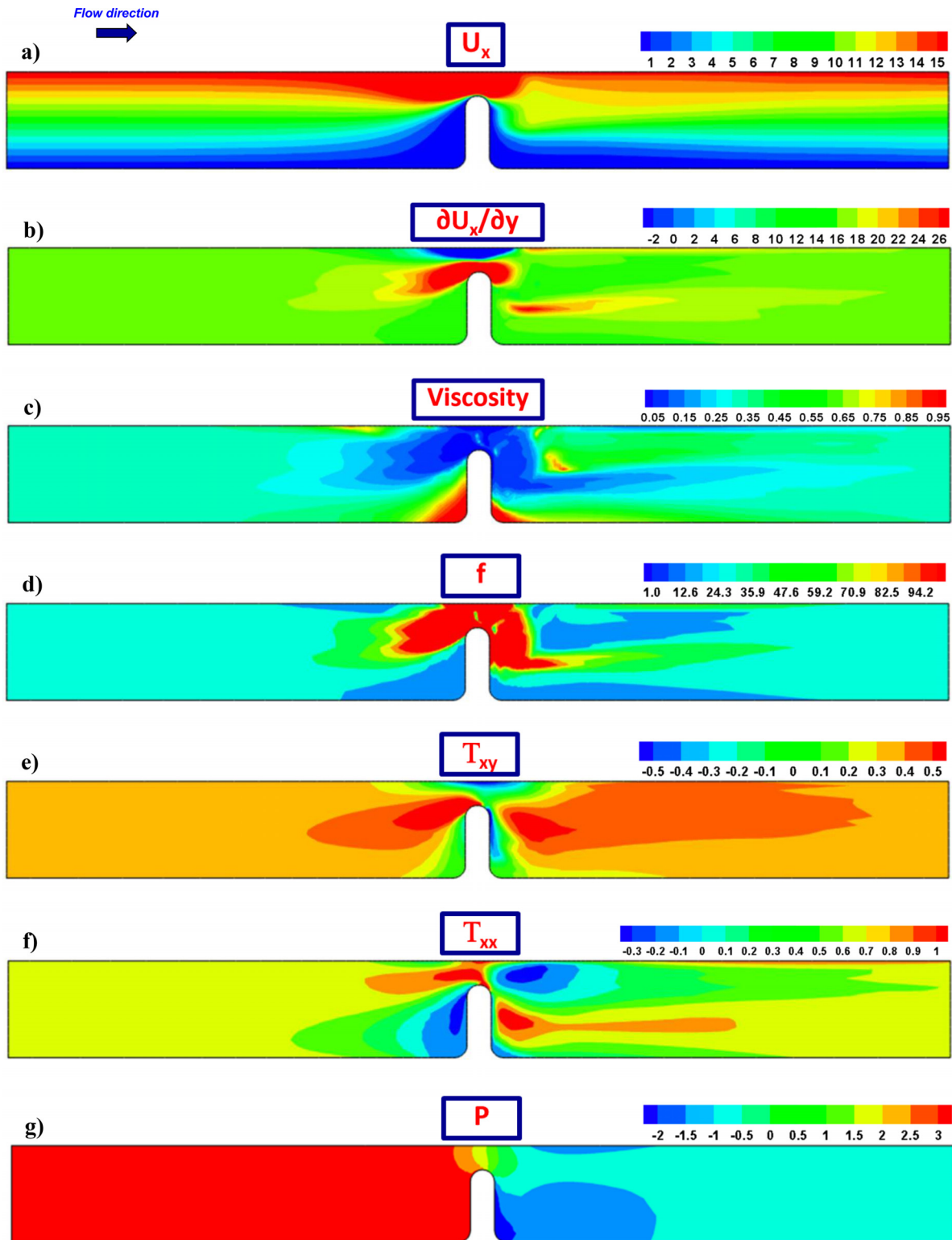


FIG. 10. (a) Velocity U_x , (b) shear rate $\partial U_x / \partial y$, (c) viscosity, (d) f -functional, (e) shear stress T_{xy} , (f) normal stress T_{xx} , and (g) pressure P fields; $\beta = 10^{-2}$, $\{\omega, \zeta_{G0}, \xi, \delta\} = \{4, 0.1136, 2.27 \times 10^{-7}, 1 \times 10^{-6}\}$; case B: non-shear-banding fluid ($\zeta = 0$).

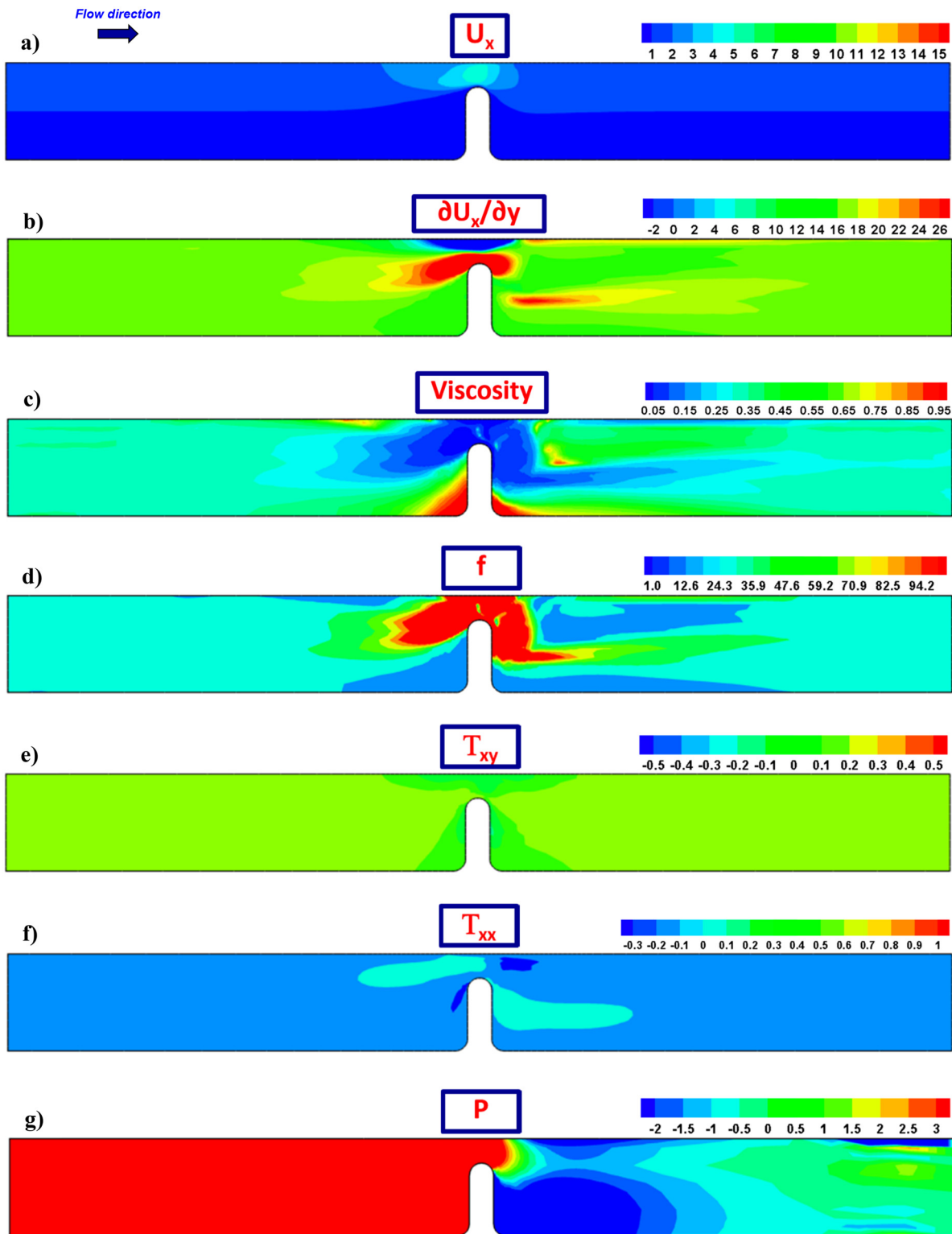


FIG. 11. (a) Velocity U_x , (b) shear rate $\partial U_x / \partial y$, (c) viscosity, (d) f -functional, (e) shear stress T_{xy} , (f) normal stress T_{xx} , and (g) pressure P fields; $\beta = 10^{-2}$, $\{\omega, \zeta_{G0}, \xi, \delta\} = \{4, 0.1136, 2.27 \times 10^{-7}, 1 \times 10^{-6}\}$; case D: shear-banding fluid ($\zeta = 3$).

04 September 2023 10:36:04

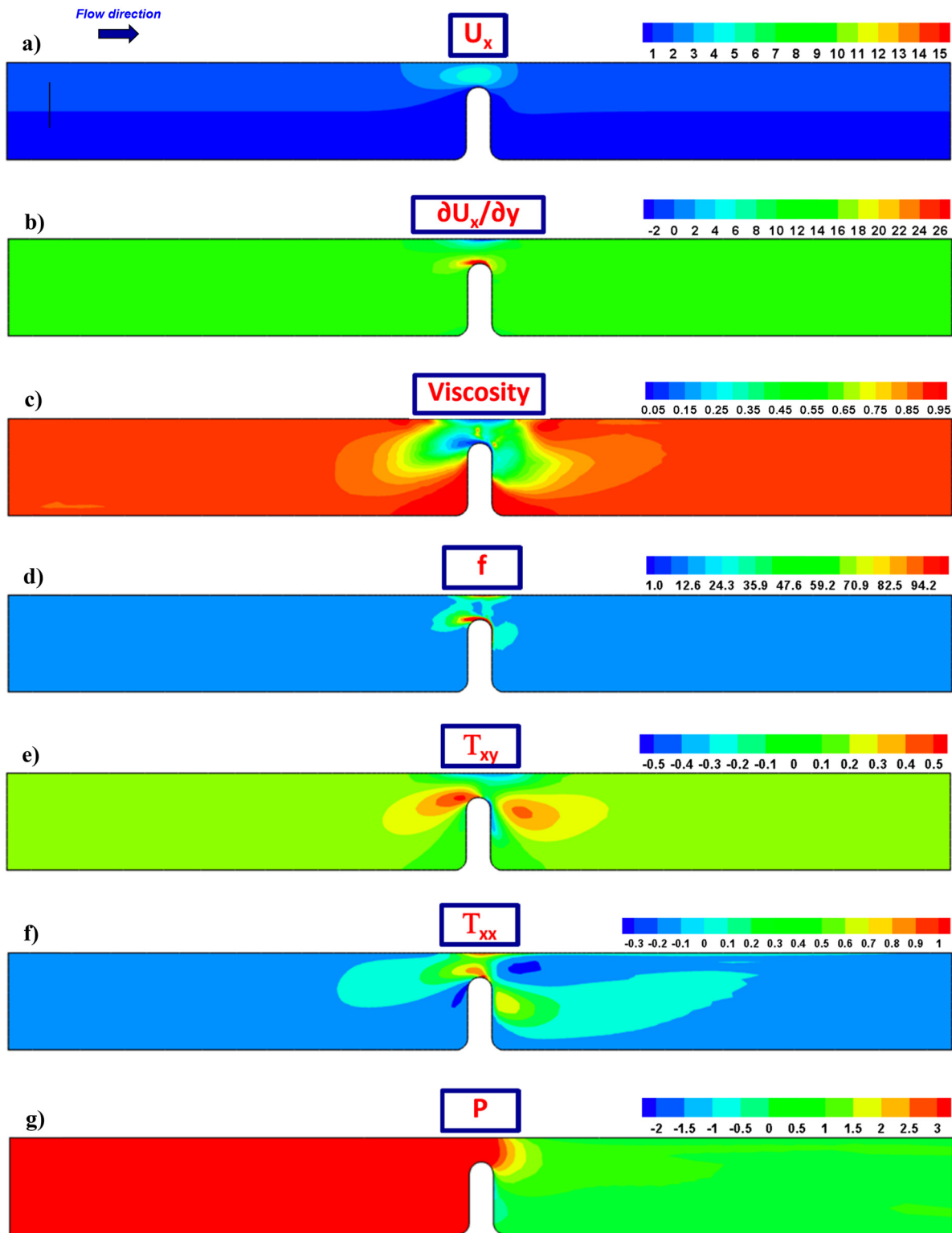


FIG. 12. (a) Velocity U_x , (b) shear rate $\partial U_x / \partial y$, (c) viscosity, (d) f -functional, (e) shear stress T_{xy} , (f) normal stress T_{xx} , and (g) pressure P fields; $\beta = 10^{-2}$, $\{\omega, \zeta_{G0}, \zeta, \delta\} = \{4, 0.1136, 2.27 \times 10^{-7}, 1 \times 10^{-6}\}$; case A: non-shear-banding fluid ($\zeta = 0$).

04 September 2023 10:36:04

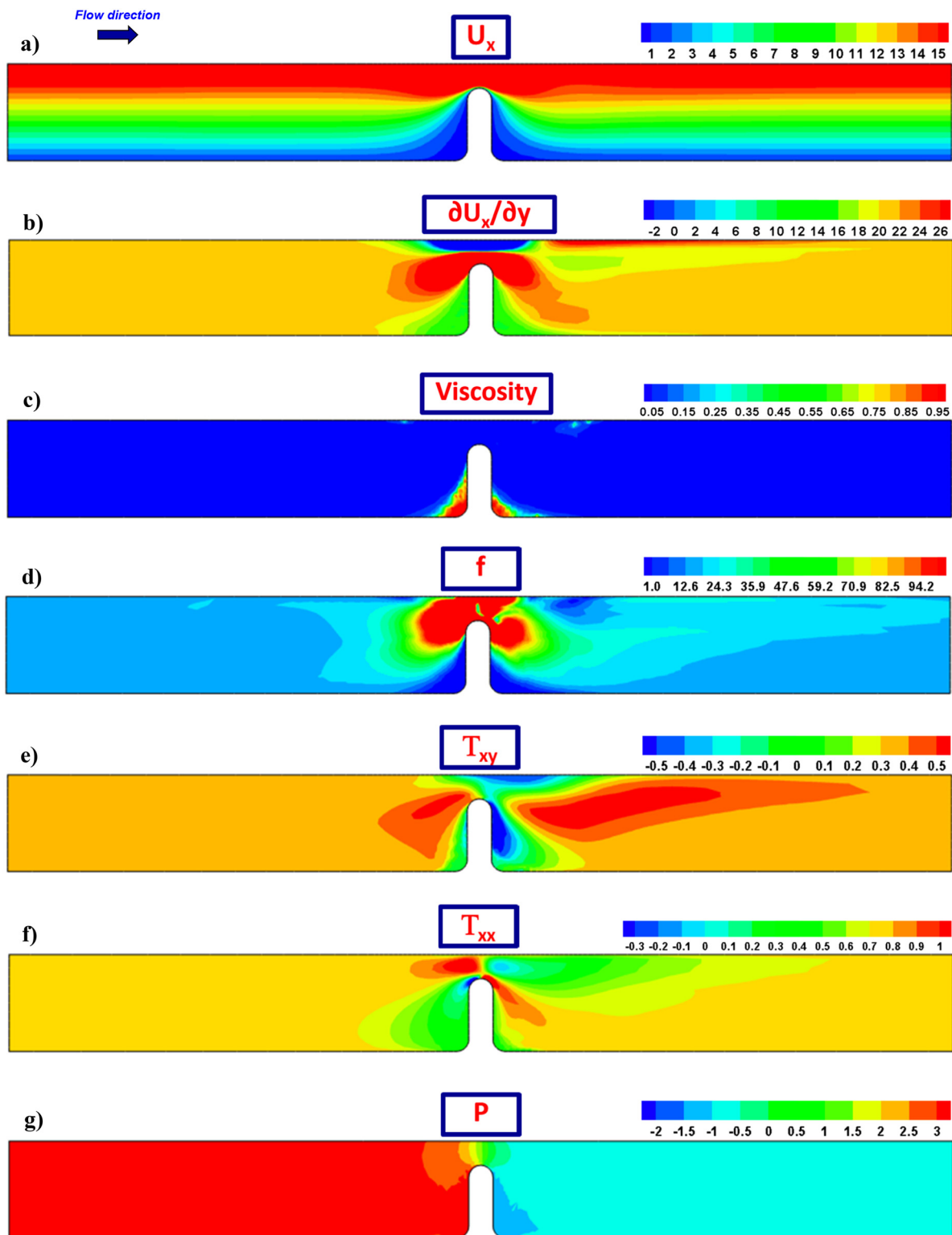


FIG. 13. (a) Velocity U_x , (b) shear rate $\partial U_x / \partial y$, (c) viscosity, (d) f -functional, (e) shear stress T_{xy} , (f) normal stress T_{xx} , and (g) P fields; $\beta = 10^{-2}$, $\{\omega, \zeta_{G0}, \zeta, \delta\} = \{4, 0.1136, 2.27 \times 10^{-7}, 1 \times 10^{-6}\}$; case C: non-shear-banding fluid ($\zeta = 0$).

04 September 2023 10:36:04

relatively strong levels of stress from the constriction zone. In this high deformation rate instance, the fluid viscosity drops dramatically, filling almost the entire geometry [Figs. 13(c) and 13(d)]. That is, with the exception of the recess regions, which acquire structured material response and appear as reduced red zones.

Unfortunately, in contrast, the high-rate shear-banding ($\zeta = 3$) case F proved to be computationally intractable for conditions of severely low solvent fraction ($\beta = 10^{-2}$). This is due to the combination of three key factors: the already extremely high flow rate $Q = 450$; the outstandingly high solute content $(1 - \beta) = 0.99$; and the additional non-linearity invoked by the non-zero shear-banding intensity parameter ($\zeta \neq 0$). Nevertheless, some evidence for the influence of ζ increase may be drawn from solutions extracted in the reduced range $0.001 \leq \zeta \leq 0.03$, but at the larger permitting solvent fraction of $\beta = 1/9$. One notes, therefore, that a final and stable steady-state solution may be gathered computationally only for a ($\zeta = 0.03$) fluid. Under these conditions, oscillations in normal stress are observed, signaling pending intractability. This implies that this fluid is in its high deformation rate stable branch of the T_{xy} flow curve, while $N_{I\text{Shear}}$ lies within its unstable branch. As these solutions do not significantly deviate from ($\zeta = 0$)-solutions, these data are withheld.

IV. CONCLUSIONS

In this work, novel solutions are reported for the shear banding of micellar systems in a complex modified planar Couette flow. Banded solutions have been attained using the BMP+ τ_p model to approximate the rheological response of highly concentrated (solvent fraction $\beta \leq 10^{-2}$) wormlike micellar solutions. In this manner, away from the constriction, simple shear flow is observed, while inhomogeneous shear-to-extensional flow is gathered about the contraction.

To contrast banding against non-banding response, two fluid representations have been chosen: a shear-banding fluid (non-monotonic flow curve with localized extrema) and a non-shear-banding fluid (monotonic flow curve). Then, three overall flow rates were fixed on the flow curve, where each flow rate corresponded to a low, intermediate, and high shear rates, respectively. Armed with these combinations, six independent instances were identified for study across two fluid types (shear-banding/non-shear-banding) and three flow rates (stable/unstable/stable).

The banding fluid in the intermediate flow rate generates segregated flow fields away from the contraction, represented via velocity, normal stress, and flow structure (viscosity or fluidity). Cross-stream fully developed samples reflect split velocity and normal stress profiles, while shear stress profiles appear constant. Such inhomogeneous response is lost in the contraction zone, where flow structure readjusts to the multiple and distributed rates encountered. This leads to a highly unstructured material response that is accelerated and stretched due to the obstruction blockage. Interestingly, pressure sustains a Couette-like form away from the contraction, with constant pressure levels that vary from upstream-to-downstream due to the inhomogeneous shear-to-extensional flow posed by the constriction. One note, in particular, is that downstream of the constriction, a banding fluid in an intermediate flow rate regime, shows a tendency to resume banded profiles, having experienced the disorder of the flow around the constriction. The plausibility of banding in $N_{I\text{Shear}}$ alone, and not within T_{xy} , is also considered an interesting and open issue to be resolved.

In contrast and apart from the region of contraction, the non-shear-banding fluid displays homogeneous velocity, shear stress, and

normal stress fields and profiles, indicating a relatively more structured material response. Flow instances in the stable branches of the flow curves, at low and high flow rates, consistently reflect simpler, non-segregated flow fields, with degrees of structure modulated by the individual deformation rate imposed. Due to the high degree of non-linearity caused by the extremely high solute concentration ($\beta \leq 10^{-2}$), the case of the banding fluid at high- Q is found to be numerically intractable. However, such predictive limitation may be addressed via larger- β solutions ($\beta = 1/9$), under which normal stress oscillations are observed as a signal of pending intractability. The implication here is that this fluid is in its high deformation rate stable branch of the T_{xy} flow curve, while $N_{I\text{Shear}}$ lies within its unstable branch.

The findings presented in this manuscript suggest new avenues of research, such as the localization in extensional deformation. This phenomenon is relevant to extension necking in wormlike micellar solutions,^{9,10} contraction,¹⁵ and pipe flows.⁴⁰ Future studies will focus on these topics.

DEDICATION

This paper is dedicated to Professor Roger I. Tanner on the occasion of his 90th birthday.

ACKNOWLEDGMENTS

J.E.L.-A. acknowledges the support from Consejo Nacional de Ciencia y Tecnología [CONAHCYT, Mexico—Grant No. CF-2023-I-318 “Reología computacional de fluidos complejos: determinación de propiedades reológicas extensionales de mucosa y generación de biomarcadores para la prevención y tratamiento de enfermedades respiratorias (COVID-19 y EPOC)”] and from Universidad Nacional Autónoma de México UNAM (Grant Nos. PAPIIT IA102022 and PAIP 5000-9172 Facultad de Química). J.E.L.-A. and O.M. acknowledge the support from UNAM under the project with Grant No. PAPIIT IN100623. H.R.T.-J. acknowledges the support of Professor Nithiarasu, Associate Dean—Research, Innovation and Impact (RII), Faculty of Science and Engineering, Swansea University, UK.

AUTHOR DECLARATIONS

Conflict of Interest

The authors have no conflicts to disclose.

Author Contributions

J. Esteban López-Aguilar: Conceptualization (lead); Data curation (lead); Formal analysis (lead); Funding acquisition (lead); Investigation (lead); Methodology (lead); Project administration (lead); Resources (lead); Writing – original draft (lead); Writing – review & editing (lead). **Hamid Reza Tamaddon Jahromi:** Formal analysis (equal); Resources (equal); Writing – review & editing (equal). **Octavio Manero:** Formal analysis (equal); Funding acquisition (equal); Writing – review & editing (equal).

DATA AVAILABILITY

The data that support the findings of this study are available from the corresponding author upon reasonable request.

REFERENCES

- ¹V. J. Anderson, J. R. A. Pearson, and E. S. Boek, "The rheology of worm-like micellar fluids," *Rheol. Rev.* **1**, 217–253 (2006).
- ²M. E. Cates and S. M. Fielding, "Rheology of giant micelles," *Adv. Phys.* **55**, 799–879 (2006).
- ³P. D. Olmsted, "Perspectives on shear banding in complex fluids," *Rheol. Acta* **47**, 283–300 (2008).
- ⁴S. Manneville, "Recent experimental probes of shear banding," *Rheol. Acta* **47**, 301–318 (2008).
- ⁵G. Ovarlez, S. Rodts, X. Chateau, and P. Coussot, "Phenomenology and physical origin of shear localization and shear banding in complex fluids," *Rheol. Acta* **48**, 831–844 (2009).
- ⁶T. Divoux, M. A. Fardin, S. Manneville, and S. Lerouge, "Shear banding of complex fluids," *Annu. Rev. Fluid Mech.* **48**, 81–103 (2016).
- ⁷J. R. A. Pearson, "Flow curves with a maximum," *J. Rheol.* **38**, 309–331 (1994).
- ⁸N. Germann, A. K. Gurnon, L. Zhou, L. P. Cook, A. N. Beris, and N. J. Wagner, "Validation of constitutive modeling of shear banding, threadlike wormlike micellar fluids," *J. Rheol.* **60**, 983–999 (2016).
- ⁹S. M. Fielding, "Triggers and signatures of shear banding in steady and time-dependent flows," *J. Rheol.* **60**, 821–834 (2016).
- ¹⁰M. Cromer, L. P. Cook, and G. H. McKinley, "Extensional flow of wormlike micellar solutions," *Chem. Eng. Sci.* **64**, 4588–4596 (2009).
- ¹¹M. Cromer and L. P. Cook, "A study of pressure-driven flow of wormlike micellar solutions through a converging/diverging channel," *J. Rheol.* **60**, 953 (2016).
- ¹²J. E. López-Aguilar, M. F. Webster, H. R. Tamaddon-Jahromi, and O. Manero, "On shear-banding and wormlike micellar system response under complex flow," *Ann. Trans. Nord. Soc. Rheol.* **25**, 197–203 (2017).
- ¹³S. Hooshyar and N. Germann, "Shear banding in 4:1 planar contraction," *Polymers* **11**, 417 1–16 (2019).
- ¹⁴S. Varchanis, S. G. Haward, J. Tsamopoulos, and A. Q. Shen, "Evaluation of constitutive models for shear-banding wormlike micellar solutions in simple and complex flows," *J. Non-Newtonian Fluid Mech.* **307**, 104855 (2022).
- ¹⁵E. J. Nodoushan, Y. J. Lee, G. H. Lee, and N. Kim, "Quasi-static secondary flow regions formed by microfluidic contraction flows of wormlike micellar solutions," *Phys. Fluids* **33**, 093112 (2021).
- ¹⁶P. Fischer and H. Rehage, "Non-linear flow properties of viscoelastic surfactant solutions," *Rheol. Acta* **36**, 13–27 (1997).
- ¹⁷C. J. Pipe, N. J. Kim, P. A. Vazquez, L. P. Cook, and G. H. McKinley, "Wormlike micellar solutions: II. Comparison between experimental data and scission model predictions," *J. Rheol.* **54**, 881–913 (2010).
- ¹⁸P. D. Olmsted, O. Radulescu, and C. Y. F. Lu, "Johnson-Segalman model with a diffusion term in a cylindrical Couette flow," *J. Rheol.* **44**, 257–275 (2000).
- ¹⁹D. Vlassopoulos and S. G. Hatzikiriakos, "A generalized Giesekus constitutive model with retardation time and its association to the spurt effect," *J. Non-Newtonian Fluid Mech.* **57**, 119–136 (1995).
- ²⁰A. K. Gurnon and N. J. Wagner, "Large amplitude oscillatory shear (LAOS) measurements to obtain constitutive equation model parameters: Giesekus model of banding and nonbanding wormlike micelles," *J. Rheol.* **56**, 333–351 (2012).
- ²¹P. A. Vazquez, G. H. McKinley, and L. P. Cook, "A network scission model for wormlike micellar solutions I. Model formulations and viscometric flow predictions," *J. Non-Newtonian Fluid Mech.* **144**, 122–139 (2007).
- ²²N. Germann, L. P. Cook, and A. N. Beris, "Nonequilibrium thermodynamic modeling of the structure and rheology of concentrated wormlike micellar solutions," *J. Non-Newtonian Fluid Mech.* **196**, 51–57 (2013).
- ²³P. Sollich, "Rheological constitutive equation for a model of soft glassy materials," *Phys. Rev. E* **58**, 738–759 (1998).
- ²⁴R. Radhakrishnan and S. M. Fielding, "Shear banding in large amplitude oscillatory shear (LAOS) strain and LAOS stress of soft glassy materials," *J. Rheol.* **62**, 559 (2018).
- ²⁵G. Ianniruberto and G. Marrucci, "Shear banding in Doi-Edwards fluids," *J. Rheol.* **61**, 93–106 (2017).
- ²⁶R. L. Moorcroft and S. M. Fielding, "Shear banding in time-dependent flows of polymers and wormlike micelles," *J. Rheol.* **58**, 103–147 (2014).
- ²⁷S. Dutta and M. D. Graham, "Mechanistic constitutive model for wormlike micelle solutions with flow-induced structure formation," *J. Non-Newtonian Fluid Mech.* **251**, 97–106 (2018).
- ²⁸R. J. Hommel and M. D. Graham, "Constitutive modeling of dilute wormlike micelle solutions: Shear-induced structure and transient dynamics," *J. Non-Newtonian Fluid Mech.* **295**, 104606 (2021).
- ²⁹J. E. López-Aguilar, M. F. Webster, H. R. Tamaddon-Jahromi, and O. Manero, "Predictions for circular contraction-expansion flows with viscoelastic & thixotropic fluids," *J. Non-Newtonian Fluid Mech.* **261**, 188–210 (2018).
- ³⁰J. E. López-Aguilar, O. Resendiz-Tolentino, H. R. Tamaddon-Jahromi, M. Ellero, and O. Manero, "Flow past a sphere: Numerical predictions of thixoviscoelastic wormlike micellar solutions," *J. Non-Newtonian Fluid Mech.* **309**, 104902 (2022).
- ³¹J. P. García-Sandoval, O. Manero, F. Bautista, and J. E. Puig, "Inhomogeneous flows and shear-banding formation in micellar solutions: Predictions of the BMP model," *J. Non-Newtonian Fluid Mech.* **179–180**, 43–54 (2012).
- ³²J. E. López-Aguilar, M. F. Webster, H. R. Tamaddon-Jahromi, and O. Manero, "A new constitutive model for worm-like micellar systems—Numerical simulation of confined contraction-expansion flows," *J. Non-Newtonian Fluid Mech.* **204**, 7–21 (2014).
- ³³C. Sasmal, "Flow of wormlike micellar solutions through a long micropore with step expansion and contraction," *Phys. Fluids* **32**, 013103 (2020).
- ³⁴J. P. Cunha, P. R. de Souza Mendes, and I. R. Siquera, "Pressure-driven flows of a thixotropic viscoplastic material: Performance of a novel fluidity-based constitutive model," *Phys. Fluids* **32**, 123104 (2020).
- ³⁵D. Broboana, C. S. Ionescu, and C. Balan, "Numerical modelling of the shear banding flow in the proximity of micro-structures," in *10th International Symposium on Advanced Topics in Electrical Engineering (ATEE)*, Bucharest, Romania (Institute of Electrical and Electronics Engineers, 2017), pp. 483–486.
- ³⁶Z. Tadmor and C. G. Gogos, *Principles of Polymer Processing* (Wiley-Interscience, 2006).
- ³⁷J. E. López-Aguilar, M. F. Webster, H. R. Tamaddon-Jahromi, and O. Manero, "High-Weissenberg predictions for micellar fluids in contraction-expansion flows," *J. Non-Newtonian Fluid Mech.* **222**, 190–208 (2015).
- ³⁸J. E. López-Aguilar, M. F. Webster, H. R. Tamaddon-Jahromi, and O. Manero, "Convoluting models and high-Weissenberg predictions for micellar thixotropic fluids in contraction-expansion flows," *J. Non-Newtonian Fluid Mech.* **232**, 55–66 (2016).
- ³⁹K. A. Carter, J. M. Girkin, and S. M. Fielding, "Shear banding in large amplitude oscillatory shear (LAOS) strain and LAOS stress of polymers and wormlike micelles," *J. Rheol.* **60**, 883–904 (2016).
- ⁴⁰M. M. Britton, R. W. Mair, R. K. Lambert, and P. T. Callaghan, "Transition to shear banding in pipe and Couette flow of wormlike micellar solutions," *J. Rheol.* **43**, 897–909 (1999).